JUL 03 1996

NAS 1.29/3-2: 96-02

NASA Tech Briefs

National Aeronautics and
Space Administration

Electronic Components and Circuits

Electronic Systems

Physical Sciences

Materials

Computer Programs

Mechanics

Machinery

Fabrication Technology

Mathematics and Information Sciences

Life Sciences

96-02

Am 96034243

February 1996

INTRODUCTION

Tech Briefs are short announcements of new technology derived from the research and development activities of the National Aeronautics and Space Administration. These Briefs emphasize information considered likely to be transferable across industrial, regional, or disciplinary lines and are issued to encourage commercial application.

Availability of NASA Tech Briefs and TSP's

Distribution of NASA Tech Briefs, a monthly periodical publication, is limited to engineers in U.S. Industry and to other domestic technology transfer agents. Requests for individual Tech Briefs or for Technical Support Packages (TSP's) announced herein should be addressed to

NASA Center for AeroSpace Information
Technology Transfer Office
800 Elkridge Landing Rd.
Linthicum Heights, MD 21090-2934
Telephone No. (301) 621-0245

Please reference the three-letter, five-digit control number located at the end of each Tech Brief. Information on NASA's Technology Utilization Program, its documents, and services is also available at the same facility.

Technology Utilization Officers and Patent Counsels are located at NASA field installations to provide technology-transfer access to industrial users. Inquiries can be made by writing to NASA field installations listed below.

Technology Utilization Officers and Patent Counsels

Ames Research Center
Technology Utilization Officer
Mail Code 223-3
Moffett Field, CA 94035

Patent Counsel
Mail Code 200-11
Moffett Field, CA 94035

Goddard Space Flight Center
Technology Utilization Officer
Mail Code 702-1
Greenbelt, MD 20771

Patent Counsel
Mail Code 204
Greenbelt, MD 20771

Lyndon B. Johnson Space Center
Technology Utilization Officer
Mail Code IC-4
Houston, TX 77058

Patent Counsel
Mail Code AL3
Houston, TX 77058

John F. Kennedy Space Center
Technology Utilization Officer
Mail Stop PT-PMO-A
Kennedy Space Center, FL 32899

Patent Counsel
Mail Code PT-PAT
Kennedy Space Center, FL 32899

Langley Research Center
Technology Utilization Officer
Mail Stop 143
Hampton, VA 23665

Patent Counsel
Mail Code 279
Hampton, VA 23665

Lewis Research Center
Technology Utilization Officer
Mail Stop 7-3
21000 Brookpark Road
Cleveland, OH 44135

Patent Counsel
Mail Code LE-LAW
21000 Brookpark Road
Cleveland, OH 44135

Jet Propulsion Laboratory
Technology Utilization Officer
Mail Stop 156-211
4800 Oak Grove Drive
Pasadena, CA 91109

NASA Resident Office-JPL
Technology Utilization Officer
Mail Stop 180-801
4800 Oak Grove Drive
Pasadena, CA 91109

Patent Counsel
Mail Code 180-801
4800 Oak Grove Drive
Pasadena, CA 91109

George C. Marshall Space Flight Center
Technology Utilization Officer
Code AT01
Marshall Space Flight Center,
AL 35812

Patent Counsel
Mail Code CC01
Marshall Space Flight Center,
AL 35812

John C. Stennis Space Center
Technology Utilization Officer
Code HA-30
Stennis Space Center, MS 39529

NASA Headquarters
Technology Utilization Officer
Code CU
Washington, DC 20546

Assistant General Counsel for Patent Matters
Code GP
Washington, DC 20546

Dryden Flight Research Center
Technology Utilization Officer
M/S D21-31
Bldg. 4832 Whse 7
Lilly Dr.
Edwards CA 93523

NASA TechBriefs

National Aeronautics and
Space Administration

February 1996
96-02

5 Electronic Components and Circuits

13 Electronic Systems

23 Physical Sciences

33 Materials

39 Computer Programs

43 Mechanics

51 Machinery

55 Fabrication Technology

59 Mathematics and Information Sciences

63 Life Sciences

This document was prepared under the sponsorship of the National Aeronautics and Space Administration. Neither the United States Government nor any person acting on behalf of the United States Government assumes any liability resulting from the use of the information contained in this document, or warrants that such use will be free from privately owned rights.

BLANK PAGE

Electronic Components and Circuits

Hardware, Techniques, and Processes

7 Current-Sharing Control in a Multisection Power Converter
7 Micromachined Ion Accelerators
8 Open-Structure Mixer for Detection of Hydroxyl
9 Constant-Current Source for Measuring Low Resistances
10 SNS Devices With Pinhole-Defined Active Regions

BLANK PAGE

Current-Sharing Control in a Multisection Power Converter

Imbalances among currents in different sections are suppressed.

Lewis Research Center, Cleveland, Ohio

A current-sharing control scheme suppresses imbalances among the currents flowing in different sections of a multiple-section power converter. The imbalance problem arises because power converters that handle more than a few kilowatts are frequently divided into several sections called "slices"; each section of such a converter supplies a portion of the overall load current. If a condition such as slightly higher susceptibility to saturation of an inductor exists in one slice, regenerative effects can cause that section to carry a larger share of the load current than the other slices do. The result of this imbalance can be decreased conversion efficiency, overstressed components, and/or saturation of an inductor.

The current-sharing control scheme can be applied to a power converter in which the raw input power to each of *N* slices is switched on and off in pulses that are interleaved under timing control by an *N*-phase oscillator so that each slice nominally carries 1/*N* of the total current (see figure). The pulses in all the slices are of the same duration, which is adjusted by a current- or voltage-feedback control circuit to maintain the total output current or voltage, averaged over one or a few oscillator cycle(s), at the desired value. In the absence of current-sharing control, no attempt is made to measure or control the currents in individual slices, even though the currents can become imbalanced.

In the current-sharing control scheme, an additional current-feedback control loop is added to each slice. The actual current in each slice is compared with the average value *I*/*N* (where *I* denotes the total current contributed by all slices). The comparison yields an error voltage proportional to the difference between the actual and average values. The error voltage is added to a ramp voltage in the pulse-width modulator in the slice to adjust the duration of the pulses to remove the imbalance.

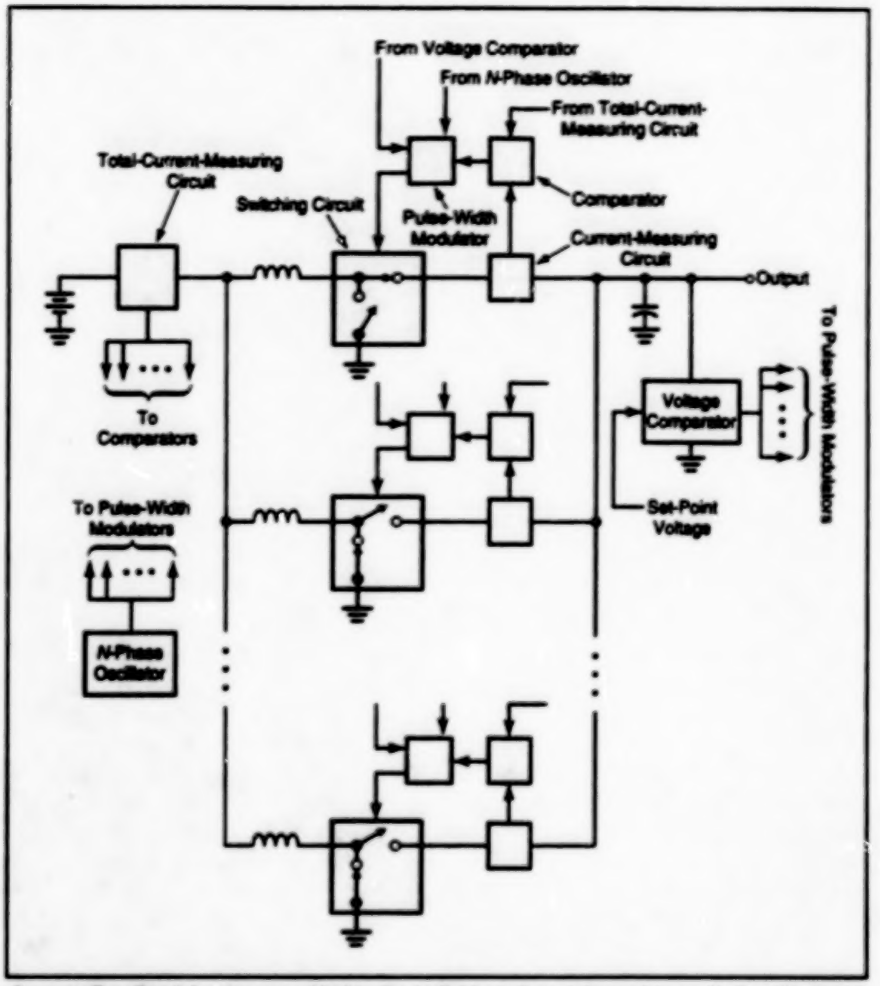

Current-Feedback Loops are added to the individual slices (phases) in an *N*-slice (*N*-phase) power converter to equalize the shares of the total current carried by the slices.

This work was done by Stan Center and Ronald J. Lenk of Space Systems/Loral for **Lewis Research Center**. *Further information is contained in a TSP [see page 1].*
LEW-15707

Micromachined Ion Accelerators

Advantages would include small size and weight, modularity, and compatibility with integrated circuits.

NASA's Jet Propulsion Laboratory, Pasadena, California

Proposed ion accelerators an order of magnitude smaller than the smallest now in use would be made by micromachining techniques like those now used to fabricate integrated circuits. Originally intended for use as thrusters aboard small spacecraft (the concept of "ion thruster on a chip"), these ion accelerators could also be used as sources of ion beams for industrial processes. An ion accelerator of this type could be combined with integrated electronic control and power circuitry, plus similarly miniaturized valves and other mechanisms for regulating the flow of gas used to generate the ions — all micromachined on a single chip. The resulting combination of small size and modularity would provide flexibility for tailoring characteristics of ion sources for specific applications; for example, one could construct an array of many such devices to obtain a large ion source or could position multiple devices to obtain a desired ion-beam pattern in a processing chamber.

A micromachined ion accelerator (see figure) would be built up on a substrate, using alternating layers of electrically

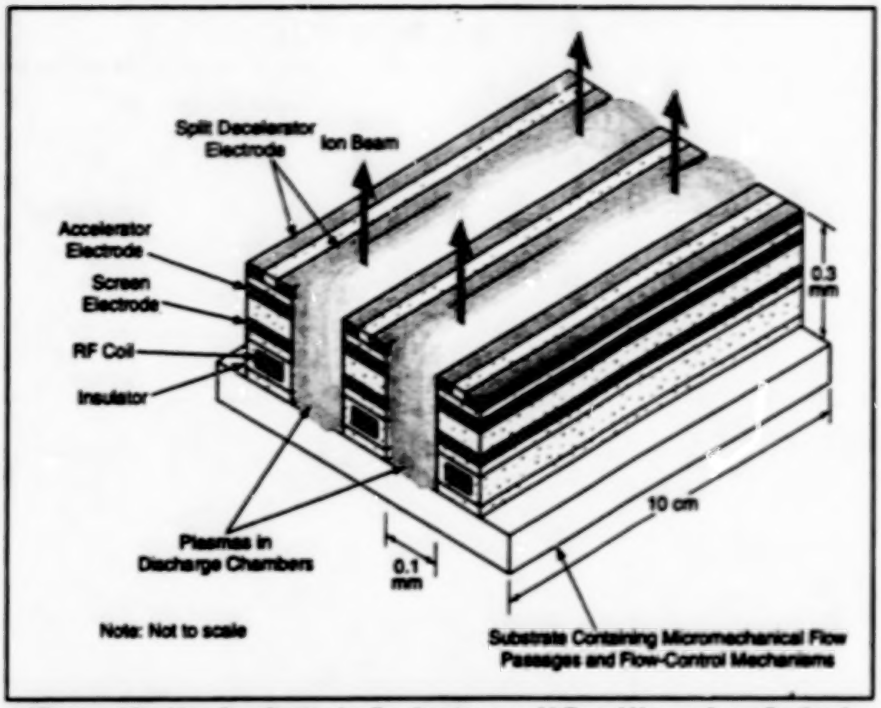

A Micromachined Ion Accelerator (an "ion thruster on a chip") would be much smaller than ion accelerators now in use. The dimensions shown here are order-of-magnitude figures for example only; dimensions could be chosen to suit specific applications.

conducting and electrically insulating materials. Typically, the overall thickness of the device, including the substrate, would be a few millimeters. The substructure containing the ion-accelerating electrodes and the discharge chamber(s) for generating the ions would be only about 300 μm thick. The long dimension of the discharge chambers in the accelerator could be any length, but would be typically several centimeters. Although the figure shows only two side-by-side linear discharge chambers, each about 100 μm wide, an accelerator could contain more such chambers, so that its width could be comparable to its length.

The device would include screen, accelerator, and decelerator electrodes separated by layers of spray-coated aluminum oxide thick enough to stand off the high voltages applied between the electrodes. The accelerator electrodes would perform the same function as that of the similarly named grids in conventional ion accelerators. The screen electrodes would collect electrons stripped from the gas in the ionization process, and an external neutralizer (not shown in the figure) would inject the collected electrons into the ion beam. The decelerator grid would be split into two pieces so that different voltages could be applied to the pieces to steer the ion beam.

The substrate would contain integral micromachined passages that would distribute the flow of gas to the discharge chamber(s), high-voltage isolators to prevent undesired discharges elsewhere than in the discharge chamber(s), and the integral micromachined flow-control mechanisms mentioned above. Of course, the gas would still have to be supplied from an external pressure vessel.

Two alternative discharge concepts are under consideration. In the device shown in the figure, the discharge would be energized by radio-frequency (RF) induction via the micromachined equivalent of a single-turn RF coil wrapped around each discharge chamber and insulated with aluminum oxide. In operation, the RF excitation in the coil would inductively couple an alternating electric field into the chamber, generating a plasma; the RF electric field would accelerate the plasma electrons to energies sufficient to ionize the gas molecules or atoms.

The other discharge concept is that of a dc discharge initiated via one or more micromachined cold-cathode emitter(s) in each discharge chamber. The leading candidate cold-cathode emitter is diamond film doped to form a forward-biased p/n junction, with boron as the p dopant and C^+ ions as the n dopant.

This work was done by John Brophy, Juergen Mueller, James Polk, and John Blandino of Caltech for **NASA's Jet Propulsion Laboratory**. *Further information is contained in a TSP [see page 1].*
NPO-19652

Open-Structure Mixer for Detection of Hydroxyl

Antenna, transmission-line, and mixer circuit elements are integrated.

NASA's Jet Propulsion Laboratory, Pasadena, California

A single structure that comprises a dielectric-filled paraboloidal reflector, a dipole antenna at the focus of the paraboloid, and a mixing circuit at the antenna has been developed for detecting electromagnetic radiation emitted by the hydroxyl radical at a frequency of 2,520 GHz (wavelength of 119 μm). This structure can be regarded as a prototype for a class of improved direct-detector and heterodyne circuits that will operate at millimeter and submillimeter wavelengths.

The design of this mixer combines (1) the established concept of a dielectric-filled paraboloidal reflector with the flat surface of the dielectric located in the focal plane of the paraboloid and a dipole antenna mounted on the dielectric at the focus with (2) the use of a novel combination of techniques to fabricate the antenna as part of an integrated circuit along with a mixing diode and the associated transmission line. The use of integrated circuitry is dictated by the small wavelengths and the consequent small sizes of the components that handle radio-frequency signals; there is no practical way to fabricate such small components individually.

The dielectric-filled paraboloidal reflector is made by grinding and polishing the paraboloidal and flat surfaces onto a slug of fused quartz, then depositing nickel, chromium, and gold on the paraboloidal surface to form the reflector. The integrated circuit is mounted on a narrow rectangular quartz chip that is, in turn, mounted on the focal-plane surface of the fused quartz (see figure). The integrated circuit includes the dipole antenna, a planar GaAs Schottky-barrier diode, an intermediate-frequency transmission line that also supplies dc bias to the diode, and a radio-frequency filter that prevents the local-oscillator and received signals from going out on the transmission line, along

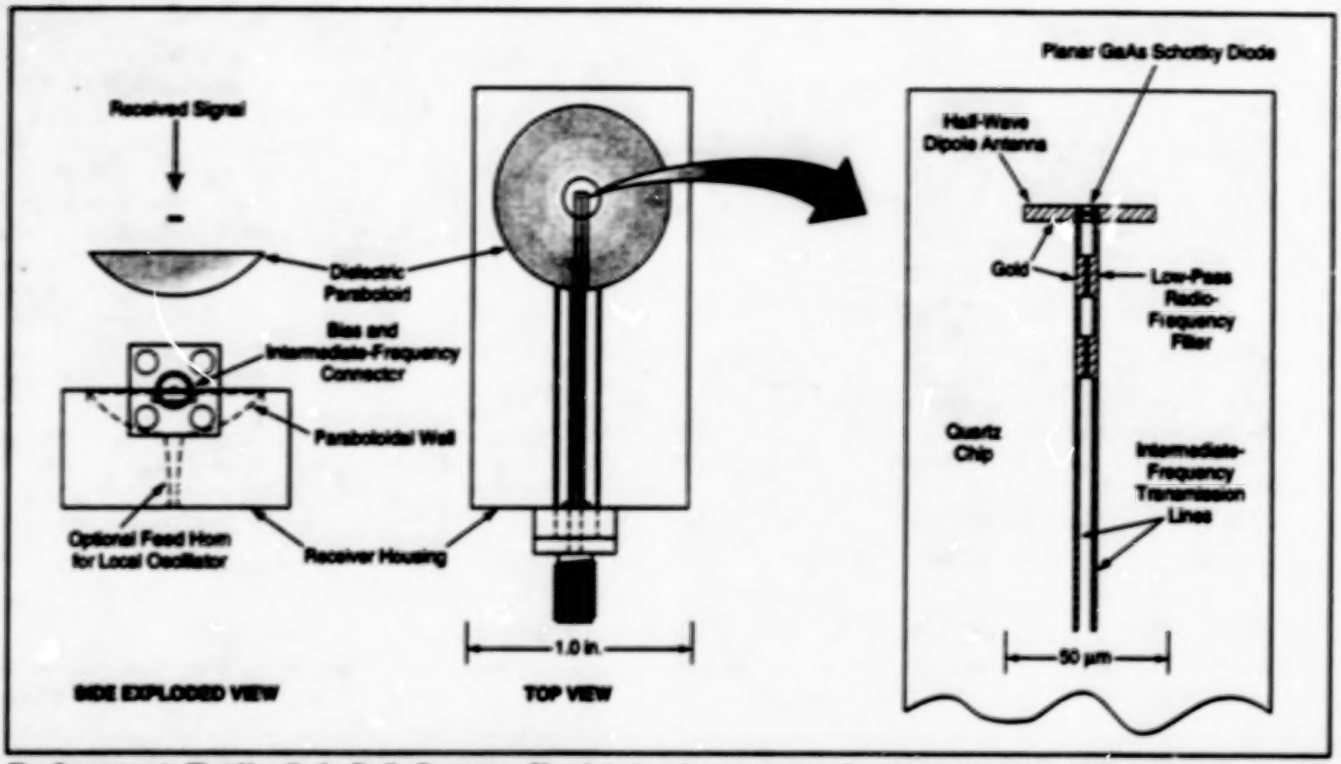

The Components That Handle the Radio-Frequency Signals in the mixer are necessarily microscopic because of the wavelengths involved and are therefore fabricated together in an integrated circuit.

with the intermediate-frequency signal, to the external receiver circuits.

To solve an earlier problem associated with device yield, the integrated circuit is fabricated as one in an array of many identical devices on a single wafer, which is then diced to obtain the individual integrated circuits. The diode and all associated signal-handling circuit elements are fabricated by use of electron-beam lithography on GaAs wafers grown by molecular-beam epitaxy. The antenna is a simple half-wave dipole made of evaporated gold, and the Schottky diode is formed at the midlength of the antenna. The radio-frequency filter is composed of alternating high- and low-impedance sections of the coplanar transmission line.

By use of a liftoff technique, the top few microns of GaAs containing the array of devices is transferred, device-side down, to a quartz wafer. The array is bonded to this substrate by use of an ultraviolet-curable optical cement. Then the GaAs around the diodes is masked and all the remaining GaAs (now on top of the antenna and intermediate-frequency transmission lines) is etched away. This leaves the original metal film of the antenna and intermediate-frequency circuitry exposed. DC contact can then be made through bonding pads at the edge of the wafer. The wafer can then be diced into individual rectangular integrated-circuit chips.

One of the separated chips is then positioned on the focal-plane surface of the quartz, with the diode (which is at the middle of the dipole) at the focal point. The chip is bonded in place by use of the ultraviolet-curable optical cement. Connections to the dc-bias lines are made via bond wires at the one edge of the chip that coincides with the edge of the fused-quartz dielectric.

A balun transformer converts the mode of propagation of the intermediate-frequency signal from that of the coplanar balanced line on the antenna wafer to that of the unbalanced coaxial line. It also transforms the 200-Ω impedance required for matching the diode to the 50-Ω impedance of an external coaxial transmission line. Wire bonds are used to connect the balun to the quartz wafer on one side and to a coaxial panel mount connector on the other.

In operation, the received and local-oscillator signals can be coupled into the reflector and antenna via a conventional beam splitter or interferometric diplexer. Optionally, the local-oscillator signal can be coupled in via a small conical feed horn and a hole in the reflective coat at the apex of the paraboloid. The paraboloidal reflector focuses the signals onto the dipole antenna, where they are directly coupled to the diode. The intermediate-frequency signal is coupled out via the coplanar lines and balun transformer.

This work was done by Peter H. Siegel of Caltech for **NASA's Jet Propulsion Laboratory.** *Further information is contained in a TSP [see page 1].*
NPO-19267

Constant-Current Source for Measuring Low Resistances

At a current of 1 A, resistances are indicated directly as voltages.

NASA's Jet Propulsion Laboratory, Pasadena, California

A constant-current source has been constructed for measuring electrical resistances up to a few ohms in power-supply equipment. By setting the current at 1 A and measuring the resulting voltage drop across an item under test, one obtains a voltage reading that is numerically equal to the resistance in ohms.

The constant-current source (see figure) includes an unregulated power supply of 10 to 12 Vdc, the specific design of which was chosen to minimize dissipation of

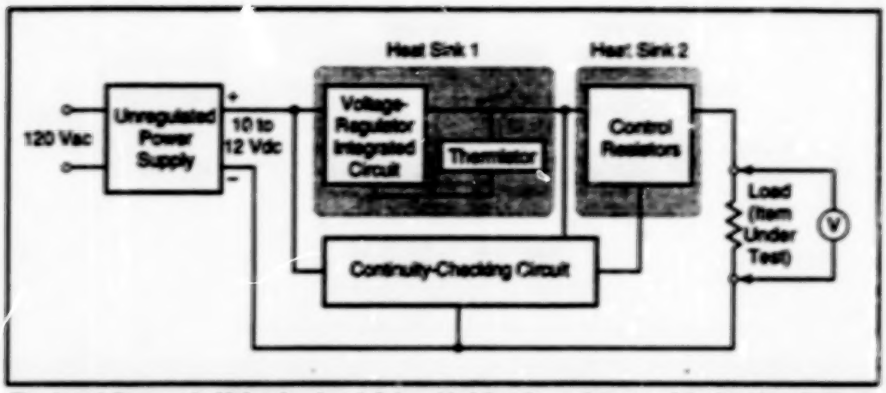

The Load Current Is Maintained at 1 A (provided that the resistance of the load is ≤ 5 Ω), so that the voltage across the load equals its resistance in ohms. The voltage is best measured by use of an autoranging, high-resolution digital voltmeter. Load resistances as small as 1 μΩ can be measured in this way.

power, to minimize arcing upon connection to a low-resistance load, and to be capable of supplying a steady output current of 1 A to a load of ≤ 5 Ω. The circuit also includes a commercial voltage-regulator integrated circuit connected to provide a constant current. This integrated circuit is mounted on a heat sink. The output current is manually adjusted to the desired constant value (e.g., 1 A) by use of a variable-control resistor mounted on a second heat sink. Both heat sinks are as large as is feasible and are thermally isolated from each other. A thermistor with negative temperature coefficient, mounted on the same heat sink as that of the voltage-regulator integrated circuit, enhances the stability of the output current.

This work was done by Robert L. Toomath of Caltech for **NASA's Jet Propulsion Laboratory**. *Further information is contained in a TSP [see page 1].*
NPO-19337

SNS Devices With Pinhole-Defined Active Regions

Junction resistances and maximum junction voltages are expected to be increased.

NASA's Jet Propulsion Laboratory, Pasadena, California

Superconductor/normal conductor/superconductor (SNS) microbridge devices with pinhole-defined active regions are undergoing development. (SNS microbridges are also known, variously, as SNS weak links and as Josephson junctions.) A device of the present type includes a thin, electrically insulating layer deposited epitaxially, with controlled formation of pinholes, on one of the two superconducting layers. The normally conducting metal is deposited epitaxially in the pinholes and on the insulating layer, forming the electrical contact between the two superconducting layers. The pinholes thus define the microbridges — the narrow, normally conductive active regions that collectively constitute the desired normally conducting "weak link." The average current density through the weak link is determined partly by the total pinhole area and the thickness of the normally conducting metal layer.

The major purpose of this development effort is to enhance performance as quantified by two figures of merit; a junction electrical resistance R_n associated with normal conduction in the microbridge(s) and a maximum junction voltage defined as I_cR_n, where I_c denotes the critical current above which superconductivity breaks down. The R_n of a typical photolithographically defined SNS device now available is < 1 Ω; it would be desirable to increase R_n to about 50 Ω to match the impedances of typical external

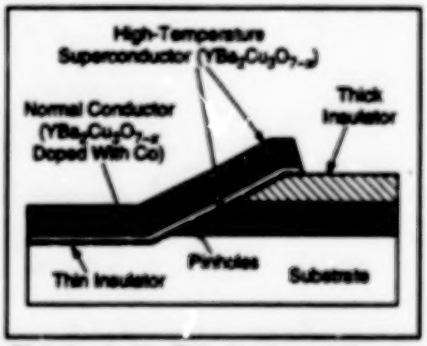

Pinholes in the Thin Insulator define the normally conducting microbridges.

circuits for efficient transfer of power. For complex reasons that exceed the scope of this article, previous approaches taken to increase R_n have been problematic and, in particular, have lead to reduced values of I_cR_n.

The practical basis for the present approach is the notion that the insulating layer in an SNS device would contain pinholes if it were made thin enough and grown under the proper conditions. If the local thickness of the insulator layer were sufficient to prevent measurable quantum-mechanical tunneling (greater than approximately 30 Å), conduction through the device would be dominated by current transport in the pinholes, and the effective active cross-sectional area of the device would then be reduced to the total pinhole area. The total pinhole area could be much smaller than the nominal area encompassed by the outline of the device, resulting in a large value of R_n.

Reducing the effective area of the device should also help solve the problems that limit the I_cR_n values of prior SNS devices. The use of a thin insulating layer with pinholes may also enable the use of a thinner layer of normally conducting metal while reducing the problems associated with nonuniform conduction through such layers.

The first attempts to fabricate SNS devices with pinhole-defined active regions are expected to involve edge-geometry SNS devices like that shown in schematic cross section in the figure. The thin pinhole insulator layer would be grown on the edge of the superconducting base electrode. The advantages of the edge-junction approach include that (1) current would flow along the high-current-density direction of the $YBa_2Cu_3O_{7-x}$ throughout the device; (2) the interfaces between the normally conducting metal and the superconductors would be formed on the longer-coherence-length surfaces perpendicular to the *a-b* planes of the $YBa_2Cu_3O_{7-x}$; and (3) very short, small-area devices could be fabricated by use of conventional optical lithography.

The pinhole-insulator approach should also work just as well with the insulator grown on top of the normally conducting metal, rather than below it. Presumably, in either case, the density of pinholes could be controlled reproducibly by sim-

ply varying the nominal average thickness of the insulator, and by varying such conditions as the temperature and the background pressure of oxygen during the deposition of the insulating material. A thin insulating layer is expected to contain pinholes because many deposited materials grow in a three-dimensional fashion, starting as islands that meet and coalesce as more material is deposited.

The superconducting electrodes in the initial experiments are expected to be made of the high-temperature superconductor $YBa_2Cu_3O_{7-x}$. The normally conducting material is expected to be $YBa_2Cu_3O_{7-x}$ doped with Co. The insulating material is expected to be Sr_2AlTaO_6. This insulating material is chosen because its relative permittivity (~25) is smaller than that of other candidate insulating materials; smaller permittivity results in smaller junction capacitances and thus higher limits on achievable operating frequencies.

This work was done by Brian D. Hunt and Jeffrey B. Barner of Caltech for **NASA's Jet Propulsion Laboratory.** *Further information is contained in a TSP [see page 1].*

NPO-19475

BLANK PAGE

Electronic Systems

Hardware, Techniques, and Processes

15 Laser-Scan Ultrasonic/Thermographic Inspection System
15 Modified-Signed-Digit Optical Computing Using Fan-Out
17 Holographic Vibration Testing With Video/Computer Imaging
17 Imaging Spectrometer With Liquid-Crystal Tunable Filter
18 Parametric Amplification for Detecting Weak Optical Signals
19 Robot for Infrared Mapping of a Large Assembly in a Vacuum
19 Dynamically Reconfigurable Optical Morphological Processor
21 Higher-Order Neural Networks Recognize Patterns

BLANK PAGE

Laser-Scan Ultrasonic/Thermographic Inspection System

This system would reveal hidden defects.

NASA's Jet Propulsion Laboratory, Pasadena, California

The laser ultrasonic/thermographic inspection system is a conceptual instrument that would be used in nondestructive inspection of large areas of structures for subsurface defects. For example, it would be operated in the field to examine aircraft and pressure vessels for hidden cracks. Unlike some other inspection apparatuses based wholly or partly on ultrasonic probing of material specimens, this system would not require contact with the inspected structure or the use of an ultrasonic-coupling medium. The instrument would obtain data in ultrasonic and thermographic C-scans over structural surfaces with contours characterized by surface normal vectors that vary by angles as large as 45°.

A high-power pulsed laser beam would be scanned across a structural surface of interest in a raster pattern, by use of a scanning mirror on piezoelectric actuators. The laser pulses would induce ultrasonic pulses that would propagate through the structure and be reflected by discontinuities. The small ultrasonic surface displacements would be measured interferometrically and would be converted to digital electronic signals for further processing. To set the length scale for the image synthesized from the scan, an interferometric proximity sensor would measure the distance from the instrument to the scanned surface.

Simultaneously, thermographic data would be collected by a thermographic-analyzer subsystem. These data would be processed to determine the reflectivity of the surface to detect surface anomalies to correct the ultrasonic measurements. The thermographic data would also be processed to monitor thermal diffusivity to obtain additional information about defects that are hidden behind the surface and manifest themselves as thermal discontinuities.

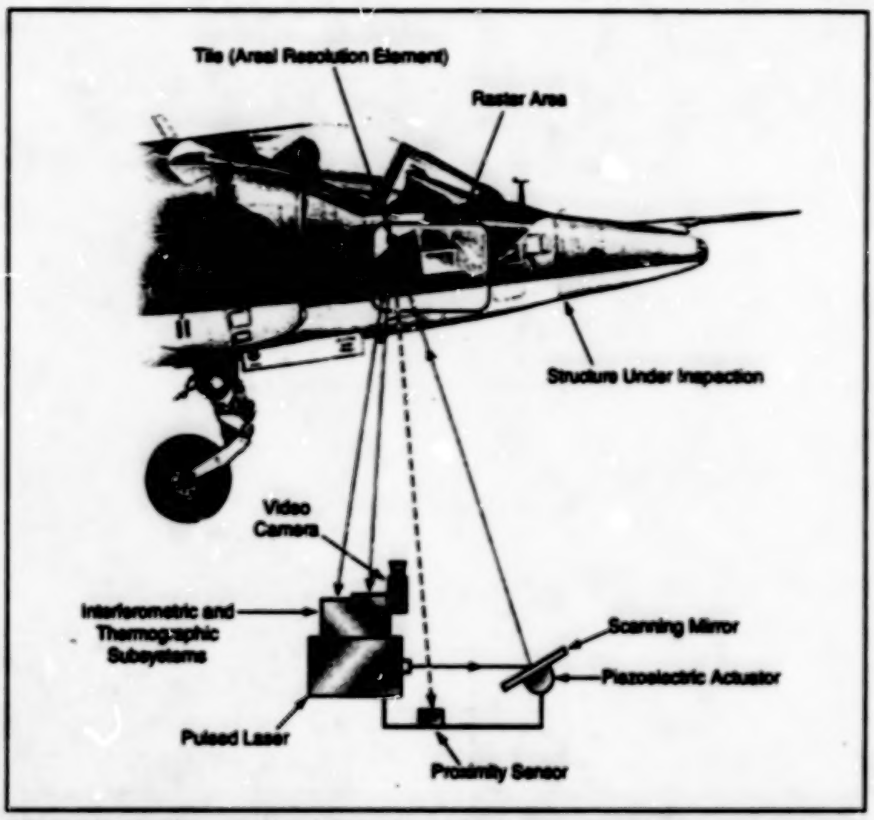

Ultrasonic vibrations would be induced by a pulsed, raster-scanned laser beam and would be measured interferometrically. The scanned surface would also be observed thermographically. The data from ultrasonic and thermographic measurements would be fused into an image of subsurface defects in the scanned structure.

An expert-system computer program would analyze the ultrasonic and thermographic data and generate a subsurface-defect image of each tile (areal resolution element) of the raster scan. A miniature video camera would provide an image of the structure and of each tile on the structure, so that each tile could be located in proper geometric relationship with the other tiles in generating the subsurface-defect image of the entire scanned area of the structure.

This work was done by Yoseph Bar-Cohen and Neville Marzwell of Caltech, Tom Chung of TRW, and Greg Carman of UCLA for NASA's Jet Propulsion Laboratory. Further information is contained in a TSP [see page 1].

NPO-19260

Modified-Signed-Digit Optical Computing Using Fan-Out

Optical fan-out elements facilitate implementation of trinary arithmetic and logic.

NASA's Jet Propulsion Laboratory, Pasadena, California

An experimental optical computing system that contains optical fan-out elements implements modified signed-digit (MSD) arithmetic and logic. MSD arithmetic partly resembles binary arithmetic: the MSD representation of a decimal digit, D_d, is given by

$$D_d = \sum_i c_i 2^i$$

where $c_i = \bar{1}$, 0, or 1.

MSD computing offers theoretical advantages, but heretofore, practical implementation has been inhibited by the need for complex optics and the smallness of achievable spatial-bandwidth products. The optical fan-out elements in this system enable discrete correlation and multiple imaging, which facilitate the implementation of MSD arithmetic and logic. In comparison with previous optical implementations of MSD arithmetic, this one is characterized by larger throughput, greater flexibility, and simpler optics.

In this system, each signed digit is associated with a square or rectangular picture element that is subdivided into three equal areas, and the value of the signed digit (1, 0,

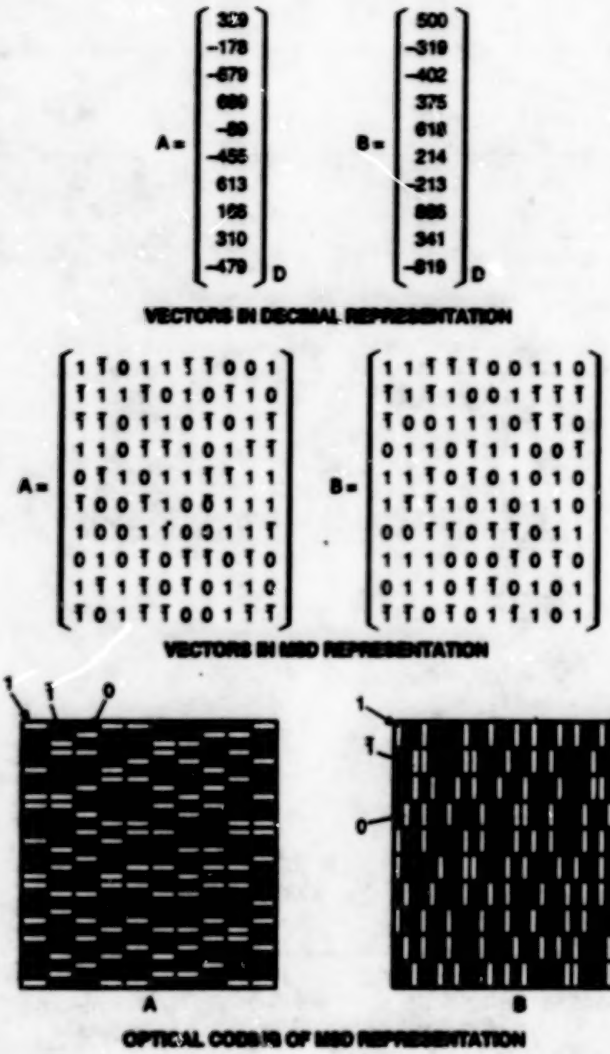

Figure 1. The Value of a Signed Digit ($\bar{1}$, 0, or 1) is represented optically by a bright spot in one of the 3 subdivisions of each square picture element: In vector A, top = 1, middle = 0, bottom = $\bar{1}$; in vector B, left = 1, middle = 0, right = $\bar{1}$.

ture elements and their trinary subdivisions.

Figure 2 schematically illustrates the optical system. A collimated laser beam is incident on overlapped masks A and B, which contain the input numbers. The axis of position coding of the signed digits in mask A is perpendicular to that in mask B, as in Figure 1. Now carrying the spatial input signal, the beam passes through a Dammann grating, which serves as the optical fan-out element. The grating generates 3 × 3 angularly multiplexed copies of the input signal. Following this, the beam is split into three subbeams on different paths by use of standard beam splitters.

On these three paths, the subbeams are Fourier-transformed and made to pass through Kernel filters (K1, K2, and K3, respectively) located in the Fourier plane of the Dammann grating. The Kernel filters are masks that contain 3 × 3 square patterns of transparent and opaque subdivisions that encode parts of the transformation rules. Physically, these filters act as spatial filters, selecting specific angular copies of the input signal. The spatially filtered subbeams then propagate through decoding masks (D1, D2, and D3, respectively). The optical processing of each subbeam effects part of the transformation. By use of beam splitters, the three subbeams are combined into an output beam bearing the complete transformation; that is, the pattern of bright spots in the output beam represents the MSD digits obtained in the arithmetic operation corresponding to the transformation rule.

This work was done by Hua-Kuang Liu of Caltech and Shaomin Zhou and Pochi Yeh of the University of California at Santa Barbara for NASA's Jet Propulsion Laboratory. Further information is contained in a TSP [see page 1].

NPO-19032

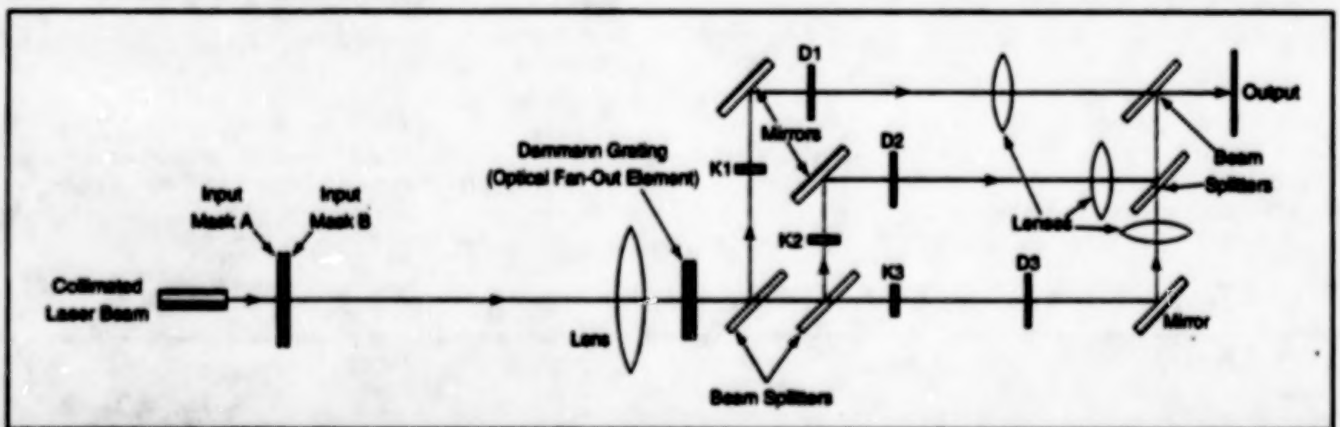

Figure 2. Spatial Filtering by the various optical elements of this system processes the input images of masks A and B into an output image in such a way as to implement a transformation rule of MSD arithmetic.

or 1) is represented by illumination in one of the subdivisions, the other two remaining dark (see Figure 1). In an MSD arithmetic operation, the input digits are processed into output digits according to a set of transformation rules, which, in the optical implementation of the present system, cause bright spots to be shifted among pic-

Holographic Vibration Testing With Video/Computer Imaging

Results are available sooner than in a prior all-photographic version.

Lewis Research Center, Cleveland, Ohio

In an improved system for holographic vibration testing, holographic interferograms that indicate the shapes of vibrational modes are recorded by a video camera under computer control. This system makes results available almost immediately, and the images can be distributed simultaneously to multiple computer terminals connected to the vibration-testing computer via a local-area network.

This system was designed to replace a prior photography-based system for identifying natural vibrational modes of propfan blades, and obviously could be adapted to similar vibration testing of other objects. The prior system yielded results more slowly because it involved photographic recording of the interferograms and thus took more time for photographic processing. Moreover, because the results were not in electronic form, they were not available simultaneously to multiple users. Yet another advantage of the improved system is that the digital image data can be stored and processed conveniently, and there is no need to store photographs.

The figure schematically illustrates the present improved system. In holographic vibration testing using either the prior or the present system, the first step is to make a conventional photographic reference hologram of the object to be tested while the object is not vibrating. After photographic development, the reference hologram is once again placed in the mount in which it was recorded. During a subsequent vibration test, the vibrating object is illuminated with the same laser beam used to make the reference hologram; the laser light reflected from the vibrating object interferes with the light in the reference holographic image, producing interference fringes indicative of the local vibrational displacement of the surface of the object from the stationary position represented by the reference image.

During a vibration test in the original propfan application, the vibrations of the propfan blade are excited by use of a nearby acoustic driver. A technician adjusts the driving frequency while watching a video image of the holographic interferogram of the propfan blade to look for clear vibration-mode shapes. Once a mode has been found, a computer commands a video frame grabber to acquire the video image of the holographic interferogram. The frame grabber digitizes the image (which is monochrome) to 512 by 480 pixels with 256 gray levels per pixel; this amounts to 245,760 8-bit bytes.

The digitized image data are passed on to the computer, where they are processed to increase contrast and bring out important details. To reduce data-storage requirements, the image data are compressed to 6,000 bytes per frame by use of the Joint Photographic Experts Group (JPEG) compression scheme with a quality factor (Q) of 25. Although the JPEG scheme at $Q = 25$ is slightly lossy, the loss in image quality is imperceptible to a human observer when an image is printed by a 300-dpi (118-dot/cm) laser printer.

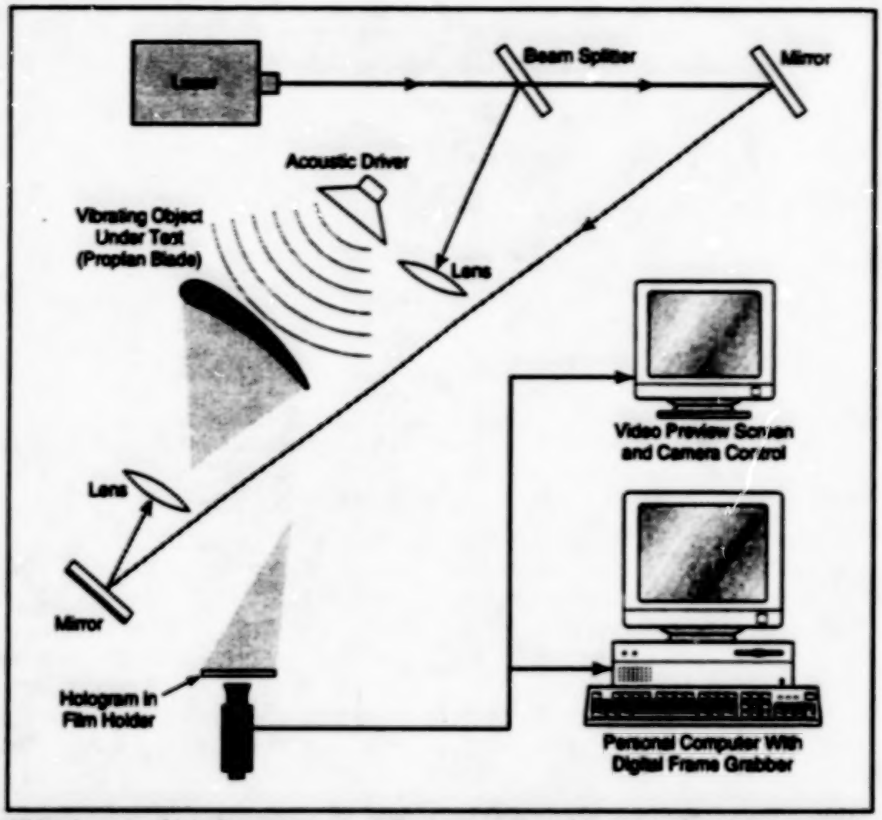

Video images of interferograms are digitized and processed for enhancement and compression. The enhanced, compressed image data can be made available via a local-area network, and paper copies can be produced easily by use of a laser printer.

This work was done by Christopher J. Miller of Lewis Research Center. Further information is contained in a TSP [see page 1].

Inquiries concerning rights for the commercial use of this invention should be addressed to the Patent Counsel, Lewis Research Center [see page 1]. Refer to LEW-16210.

Imaging Spectrometer With Liquid-Crystal Tunable Filter

A video camera collects wavelength-specific images.

NASA's Jet Propulsion Laboratory, Pasadena, California

An imaging spectrometer has been constructed from a charge-coupled-device video camera; a liquid-crystal tunable filter (LCTF) placed in front of the camera lens; and associated digital and analog control, signal-processing, and data-processing circuits (see figure). To enable operation of this instrument in the specific application for which it was

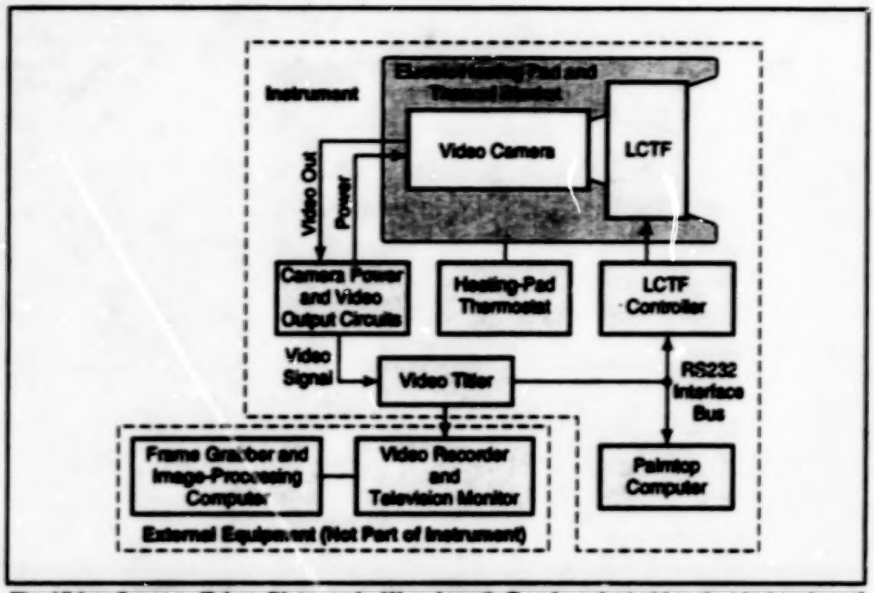

The Video Camera Takes Pictures in Wavelength Bands selected by electrical tuning of the LCTF. The heating pad, wrapped in a thermal blanket, keeps the temperature of the camera and filter above their minimum operating temperature of 5° C in cold weather.

designed (balloon flights in cold weather), the camera and LCTF are surrounded by an electric heating pad. The total operating power, excluding that consumed by the heating pad, is 16 W. The instrument weighs 4.5 kg.

The LCTF is a six-stage Lyot-type polarization interference filter that functions as an electrically tunable band-pass filter, so that images in light of different wavelength bands can be acquired by the camera at different times. Liquid crystals are used to vary the retardance of each stage in the filter. Each stage also contains a quartz retarder that serves to double the retardance of the stage. The wavelength range of the filter is 430 to 680 nm, and its transmittance of unpolarized light ranges from 8 to 17 percent. The pass band is 30 nm wide at a wavelength of 430 nm, and its width increases to 50 nm at a wavelength of 633 nm.

The tuning of the six filter stages is controlled by a microprocessor, using parameters from a calibration look-up table stored in electronic memory. Values in the table are modified to compensate for effects of temperature, so as to null out the net temperature-dependent retardance in the liquid-crystal and quartz stages. Tuning time for moving from any given pass band to any other given pass band is 50 ms. A palmtop computer running a program in the BASIC computing language is used to initialize the filter, command a sequence of filter wavelength bands, and produce band-frequency labels for superposition on the video images produced by the camera. The video images are recorded by use of an external video tape recorder and are processed by an external computer.

This work was done by Thomas G. Chrien of Caltech for **NASA's Jet Propulsion Laboratory.** *Further information is contained in a TSP [see page 1].*
NPO-19297

Parametric Amplification for Detecting Weak Optical Signals

The performances of direct-detection optical-communication receivers could be enhanced.

NASA's Jet Propulsion Laboratory, Pasadena, California

Optical-communication receivers of a proposed type would implement a high-sensitivity scheme of optical parametric amplification followed by direct detection (see figure) for reception of extremely weak signals. Neither parametric amplification nor direct detection is new by itself; what is new here is the proposal to incorporate both optical parametric amplification and direct detection into an optimized design that would enhance the effective signal-to-noise ratios during reception in the photon-starved (that is, photon-counting) regime. Such a design would eliminate the need for the complexity of a heterodyne detection scheme and would partly overcome the limitations imposed on older direct-detection schemes by noise generated in receivers and by the limits on the quantum efficiencies of photodetectors.

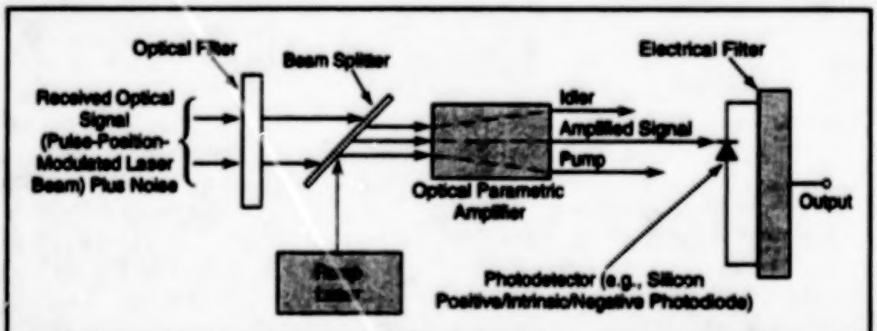

An Optical Parametric Amplifier would provide wavelength-tunable amplification to enhance the performance of a direct-detection optical receiver.

An optical parametric amplifier resembles a laser in some respects and differs in other respects, such that an optical parametric amplifier can function in the photon-starved regime, whereas a laser cannot because its operation depends on an input signal being above a threshold level. In addition, an optical parametric amplifier can operate over a wider wavelength range than a laser can, and is continuously tunable over a wide wavelength range.

Like a laser, an optical parametric amplifier includes a resonant cavity that contains a medium that responds nonlinearly to electromagnetic fields and emits coherent radiation. In general, the parametric amplification process occurs by virtue of interactions among photons in a nonlinearly responding medium: it involves the interaction between a relatively strong locally generated pump signal of frequency f_P and a weaker received signal (the signal that one seeks to amplify) of lower frequency f_S. The interaction can be characterized as a nonlinear mixing process in which the pump photons (f_P) are split into photons of both the received-signal frequency f_S and photons

of an idler frequency f_i, where $f_p = f_s + f_i$ because of conservation of photon energy. This process results in amplification and/or oscillation at both f_p and f_i.

For a given f_p, an infinite number of pairs of f_s and f_i is possible. The particular pair, and thus f_s, is determined by the phase-matching condition in the nonlinear medium. This condition can be adjusted, providing wavelength tunability in an optical parametric amplifier or oscillator. Recent improvements in some nonlinearly responding crystalline materials have opened up the possibility of constructing efficient optical parametric amplifiers. These materials include $LiNbO_3$, $KTiPO_4$, BaB_2O_4, LiB_3O_5, and $KNbO_3$.

Performances in the reception of weak pulse-position-modulated optical signals by direct-detection receivers with and without optical parametric amplification have been predicted theoretically and analyzed by computer simulation. The results of this analysis showed that in a given case, parametric amplification would enhance performance by an amount that increased with the amplifier gain, and that the use of parametric amplification could be especially helpful in the case of a photodetector of low quantum efficiency. The net enhancement is estimated to lie between 3.75 and 5.1 dB, the exact value depending on the background noise and other factors.

This work was done by Hamid Hemmati, Chien Chen, and Prakash Chakravarthi of Caltech for **NASA's Jet Propulsion Laboratory**. *Further information is contained in a TSP [see page 1].*
NPO-19514

Robot for Infrared Mapping of a Large Assembly in a Vacuum

Thermal images can be recorded from almost any direction.

NASA's Jet Propulsion Laboratory, Pasadena, California

A robotic system has been devised for use in infrared (thermal) mapping of a large assembly of equipment under test in a vacuum chamber. In the original intended application, the assembly to be thermally mapped is a spacecraft, but the system could just as well be used on integrated-circuit-fabrication equipment or other industrial equipment that operates in a vacuum.

The system includes an advanced infrared video camera, a controlled source of light, and two vacuum-rated, high-resolution, visible-light, video cameras. One of the visible-light cameras is equipped with a remotely operated zoom lens. The cameras are mounted on a pan-and-tilt mechanism on a carriage on a vertical beam in a gantry (see figure); thus, the cameras can be aimed from many different positions at many different angles.

The vertical-axis drive mechanism is of a unique lubrication-free, clean-room quality design, and can be modified easily to fit vacuum chambers with vertical dimensions up to 25 ft (7.7 m). This mechanism includes two stainless-steel drive belts, which are used to raise and lower the carriage. The mechanism can be operated in high vacuum and extreme cold.

This work was done by Douglas A. McAffee of Caltech for **NASA's Jet Propulsion Laboratory**. *Further information is contained in a TSP [see page 1].*
NPO-19578

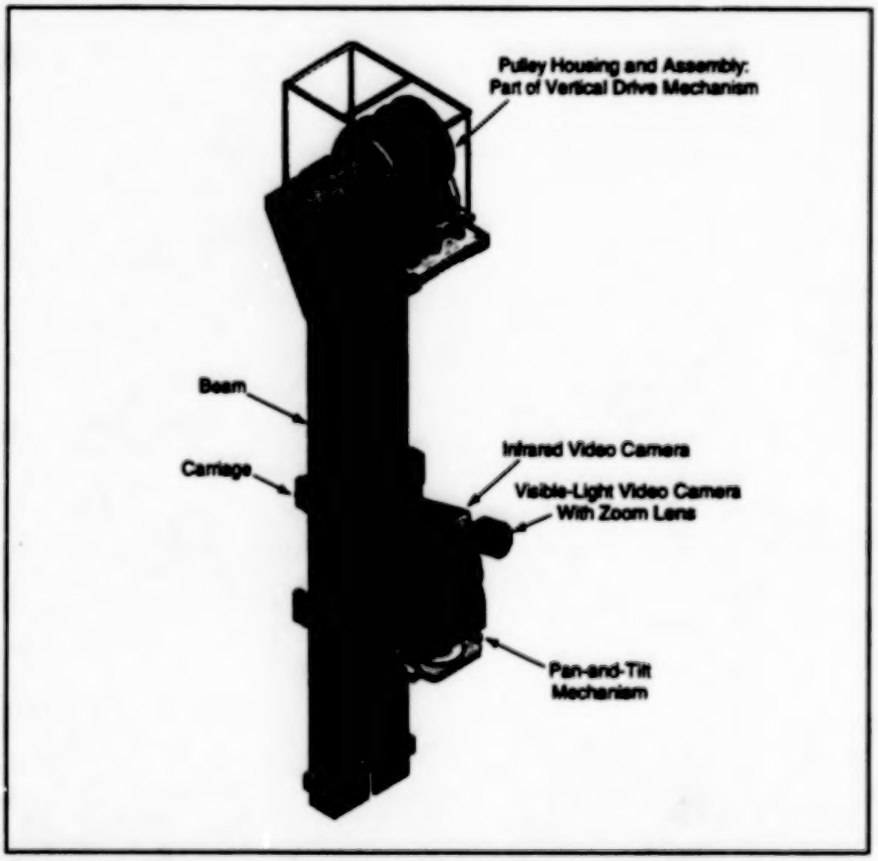

The Vertical-Axis Assembly of the Infrared-Mapping Robot contains an infrared video camera and two visible-light video cameras that can be oriented to provide stereoscopic views with scalable depth of field. The video and thermal images can be viewed, captured, and processed at a remote operator station.

Dynamically Reconfigurable Optical Morphological Processor

Reconfigurability affords an advantage over correlator-based morphological processors with fixed holographic filters.

NASA's Jet Propulsion Laboratory, Pasadena, California

An experimental optical/electronic image-processing system performs morphological processing in the optical domain. Because of the inherent parallel nature of optical processing (simultaneous processing of all parts of an image), this system operates at high speed. This system is also dynamically reconfigurable, so that it can be switched rapidly among all forms of morphological processing. Reconfigurability affords a major advantage over correlator-based optical

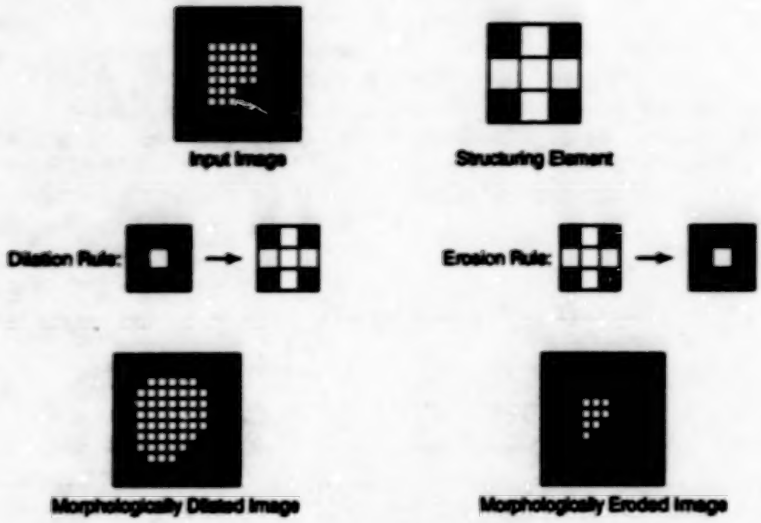

Figure 1. Dilation and Erosion are morphological operations that can be defined by use of structuring elements (in effect, few-point discrete-convolution kernels) for each pixel and its four nearest neighbors.

morphological processors in which the morphological operations are governed by fixed holographic filters.

"Morphological" as used here does not have its customary meaning. In image processing, "morphological" characterizes an operation, on each pixel of an image, that involves data from only that pixel and a few other pixels in its neighborhood. A morphological operator could also be regarded as a few-point discrete convolution over a pixel and its nearest neighbors. For example, two morphological operations that are commonly performed on binary images are called "erosion" and "dilation" (see Figure 1). Two other common operations are called "opening" (consisting of erosion followed by dilation) and "closing" (consisting of dilation followed by erosion). Opening followed by closing is useful for removing salt-and-pepper noise (isolated single black and isolated single white pixels) from a binary image.

Figure 2 schematically illustrates the present image-processing system. The input image to be processed is generated electronically by a computer, then transferred to a frame grabber, then displayed on a cathode-ray tube coupled via a fiber-optic face plate to a liquid-crystal light valve (LCLV). Thus, the LCLV is made to act as a spatial light modulator (SLM) that converts the input image into the optical domain. The input image consists of an $N \times N$ array of pixels.

A pair of lenses performs Fourier transformations between the input and the output planes. A Dammann grating between lens 1 and the Fourier-transform plane splits the impinging beams of light into an $N \times N$ array. Upon reaching the Fourier-transform plane these beams form an $N \times N$ array of Fourier spectra of the input image. An aperture pattern that represents the kernel of the desired morphological operation is placed in the Fourier-transform plane. This pattern could be, for example an opening in a central pixel and its four nearest neighbors, as in the erosion and dilation kernels of Figure 1. To enable dynamic reconfiguration, a shutter SLM is placed in the Fourier-transform plane and used to generate the pattern under computer control.

It is worth noting that since this is a parallel-processing system, every pixel in the input image is replaced, in the output image, with the pattern impressed on the shutter SLM. The output image is received by a planar array of photodetectors and thresholded. The thresholded image is displayed as output and/or sent back to the input SLM for the next iteration of processing.

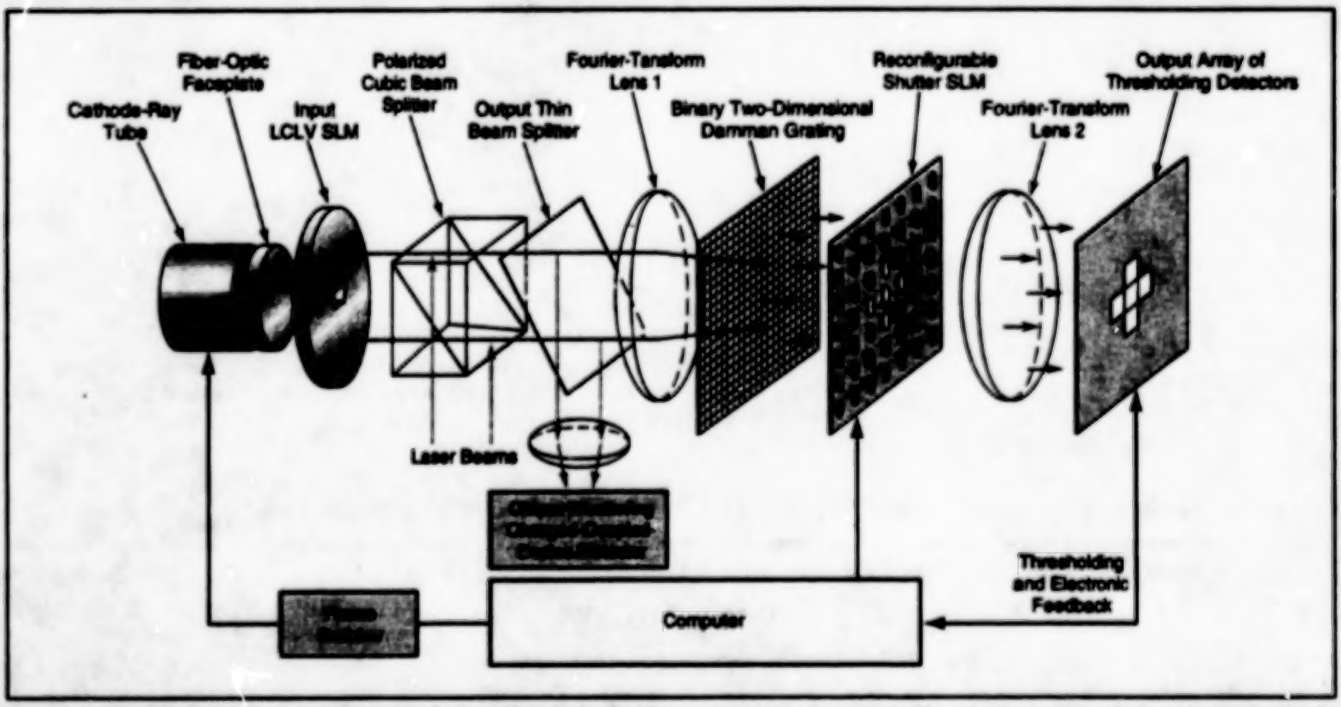

Figure 2. The Dynamically Reconfigurable Optical Morphological Processor is implemented with optical, electro-optical, and optoelectronic components, with computer-controlled input and feedback.

The process shown in Figure 2 is a dilation of a single pixel. Erosion would be performed similarly, except that the input LCLV SLM would be operated in its contrast-reversal mode. Because the system contains a feedback loop, more complex processes like opening, closing, and removal of salt-and-pepper noise can be achieved by iteratively executing a series of dilation and erosion operations. Required operations, including contrast reversal, dynamic reconfiguration, and feedback, can be accomplished via computer control.

Although the system as described thus far is designed to process binary images, the basic principle of operation can be extended to gray-scale morphological processing. The key is to utilize the thresholding decomposition technique, in which a thresholding operation is repetitively applied to a gray-scale image with a different threshold level during each successive operation. As a result, the gray-scale image would be decomposed into multiple binary images ("slices"). Each binary slice would then be processed as in the present system. All the processed binary slices would then be superposed to construct the output gray-scale image.

This work was done by Tien-Hsin Chao of Caltech for **NASA's Jet Propulsion Laboratory**. *Further information is contained in a TSP [see page 1].*

NPO-19120

Higher-Order Neural Networks Recognize Patterns

Invariance under translation, scale, and orientation can be built into a network.

Ames Research Center, Moffett Field, California

In comparison with electronic neural networks of first order, networks of higher order have enhanced capabilities to distinguish between different two-dimensional patterns and to recognize those patterns. The higher-order neural networks also have enhanced capabilities to "learn" the patterns to be recognized: they can be "trained" with far fewer examples and, therefore, in less time than is necessary to train comparable first-order neural networks.

The output of the ith output node of general neural networks is given by

$$y_i = \theta(\Sigma_j w_{ij} x_j + \Sigma_j \Sigma_k w_{ijk} x_j x_k + \Sigma_j \Sigma_k \Sigma_l w_{ijkl} x_j x_k x_l + \ldots)$$

where θ denotes a nonlinear threshold function; the ws are known variously as synaptic weights, interconnection strengths, and the like; and x_j denotes the excitation applied to the jth input node (e.g., the brightness of the jth picture element of an imaging detector onto which a pattern is projected). The order of the network is the highest order of input-excitation products included in the series; for example, if the series stops at $\Sigma_j \Sigma_k w_{ijk} x_j x_k$, then the network is of second order (see Figure 1).

A network is "trained" by an iterative process of exposing it to training sets of the pattern(s) to be recognized and adjusting the interconnection strengths until the desired outputs are obtained. Typically, for a first-order network, the process must be repeated many times with different combinations and versions of the patterns.

The great advantage of higher-order neural networks is that geometrical invariances can be built into them by use of information about the expected relationships between picture elements. In particular, a second-order neural network can be given the ability to recognize the same pattern at different locations and magnifications by imposing appropriate functional forms on the w_{ijk}. Similarly, a third-order network can be made to recognize the same pattern at different locations, magnifications, and orientations by suitable choices of the w_{ijkl}. In principle, it is not necessary to "train" such a network with differently located, magnified, and oriented versions of the same pattern (provided that the spatial resolution of the input nodes is sufficiently high): The geometrical invariances are inherent in the advance choice of constraints on the connection strengths.

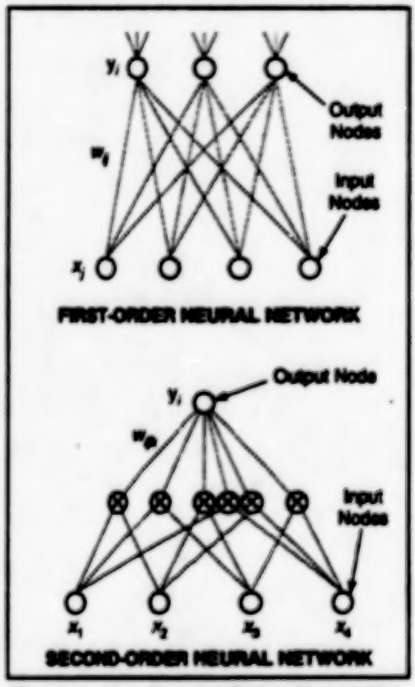

Figure 1. In a Second-Order Neural Network, excitations are multiplied in weighted pairs, then summed at the input side of the output node. In a first-order network, each excitation is weighted and added individually.

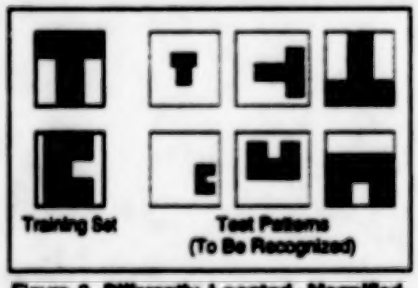

Figure 2. Differently Located, Magnified, and Orientated versions of the letters C and T were recognized by a third-order neural network after 20 training exposures to only one example of each letter.

These concepts were verified by computer simulations of the ability of a second-order and a third-order neural network to recognize the letters "C" and "T." The second-order network consisted of a 16 × 16 array of picture-element input nodes fully interconnected to a single output node. The third-order network was a 9 × 9 array of picture-element input nodes fully interconnected to a single output node. The interconnection strengths were constrained to provide the geometrical invariances. The second- order network learned to recognize both letters at various sizes and positions after only 10 training iterations on one example (one size at one position of each letter). Similarly, the third-order network was able to recognize both letters at various positions, sizes, and orientations after only 20 iterations on one example of each (see Figure 2).

This work was done by Max B. Reid, Lily Spirkovska, and Ellen Ochoa of **Ames Research Center**. *Further information is contained in a TSP [see page 1].*

This invention has been patented by NASA (U.S. Patent No. 5,333,210). Inquiries concerning nonexclusive or exclusive license for its commercial development should be addressed to the Patent Counsel, Ames Research Center [see page 1]. Refer to ARC-11961.

BLANK PAGE

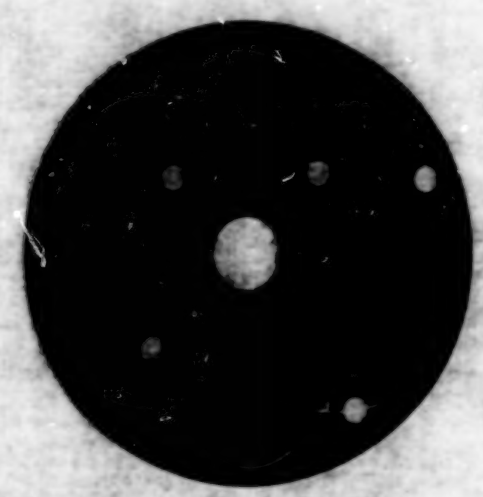

Physical Sciences

Hardware, Techniques, and Processes

25 Simultaneous Use of Zr and Mg Anodes in XPS
26 Infrared Source for Testing Thermophotovoltaic Cells
27 Compact Color Schlieren Optical System
28 Multiple-Fiber-Optic Probe for Light-Scattering Measurements
28 Measuring High Temperatures in Ceramic-Fiber Blankets
29 Gamma-Ray Imager With High Spatial and Spectral Resolution
30 Theory of Radiation-Induced Attenuation in Optical Fibers
31 Test-Aerosol Generator for Calibrating Particle Counters
32 Electrochemical Apparatus Simulates Corrosion in Crevices
32 Ultrasonic-Transmission Testing Device
32 Apparatus To Test Solvent Stress Crazing of Polymer Sheets

Books and Reports

32 Water/Ice Heat Sink With Quick-Connect Couplings

BLANK PAGE

Simultaneous Use of Zr and Mg Anodes in XPS

Previously unresolvable peaks of the electron-energy spectrum become resolvable.

Marshall Space Flight Center, Alabama

An improved x-ray source for x-ray photoelectron spectroscopy (XPS) contains both a zirconium anode with a beryllium window and a magnesium anode with an aluminum window. This x-ray source makes it possible to analyze electron-energy peaks that cannot usually be resolved when using a conventional x-ray source that contains an aluminum or magnesium anode. This source was developed specifically for use in analyzing the distributions of chemical constituents in the surface layers of specimens of 2219 aluminum alloy and, more specifically, in determining the depths of surface oxide layers and the relative proportions of aluminum and oxide in the layers. The improved x-ray source could also be used to study chemical constituents of surface layers in other material systems — for example, thin oxide films on silicon-based semiconductor devices, oxide films on alloys, and surface layers that affect the adhesion of paints or bonding materials.

Both anodes of the improved x-ray source are operated simultaneously at a potential of 15 kV and a power of 250 W each. The x-radiation from the zirconium anode includes a spectral peak at an energy of 2,042.4 eV, while that from the magnesium anode includes a spectral peak at 1,253.6 eV. Unlike the radiation from a conventional aluminum or a conventional magnesium (only) anode, this radiation provides both energy and resolution sufficient for quantitative analysis of the small concentration of aluminum metal (as little as 1/50 that of the oxide) in an oxide surface layer.

One of the reasons for this enhancement of capability is that the radiation from the improved x-ray source excites the aluminum KLL Auger spectral peaks much more effectively than does the radiation from a conventional source. The KLL Auger peaks of the metal and the oxide are separated by about 6 eV and have half-maximum widths of less than 2.5 eV. In contrast, the 2*s* and 2*p* photoelectron peaks of the metal and oxide, which are used in analysis with a conventional x-ray source, are separated by only 2 eV and have widths of almost 2 eV (see figure). Thus, the KLL Auger peaks made available by the improved x-ray source can be distinguished from each other more easily, with less subjectivity involved in interpretation of the XPS measurements.

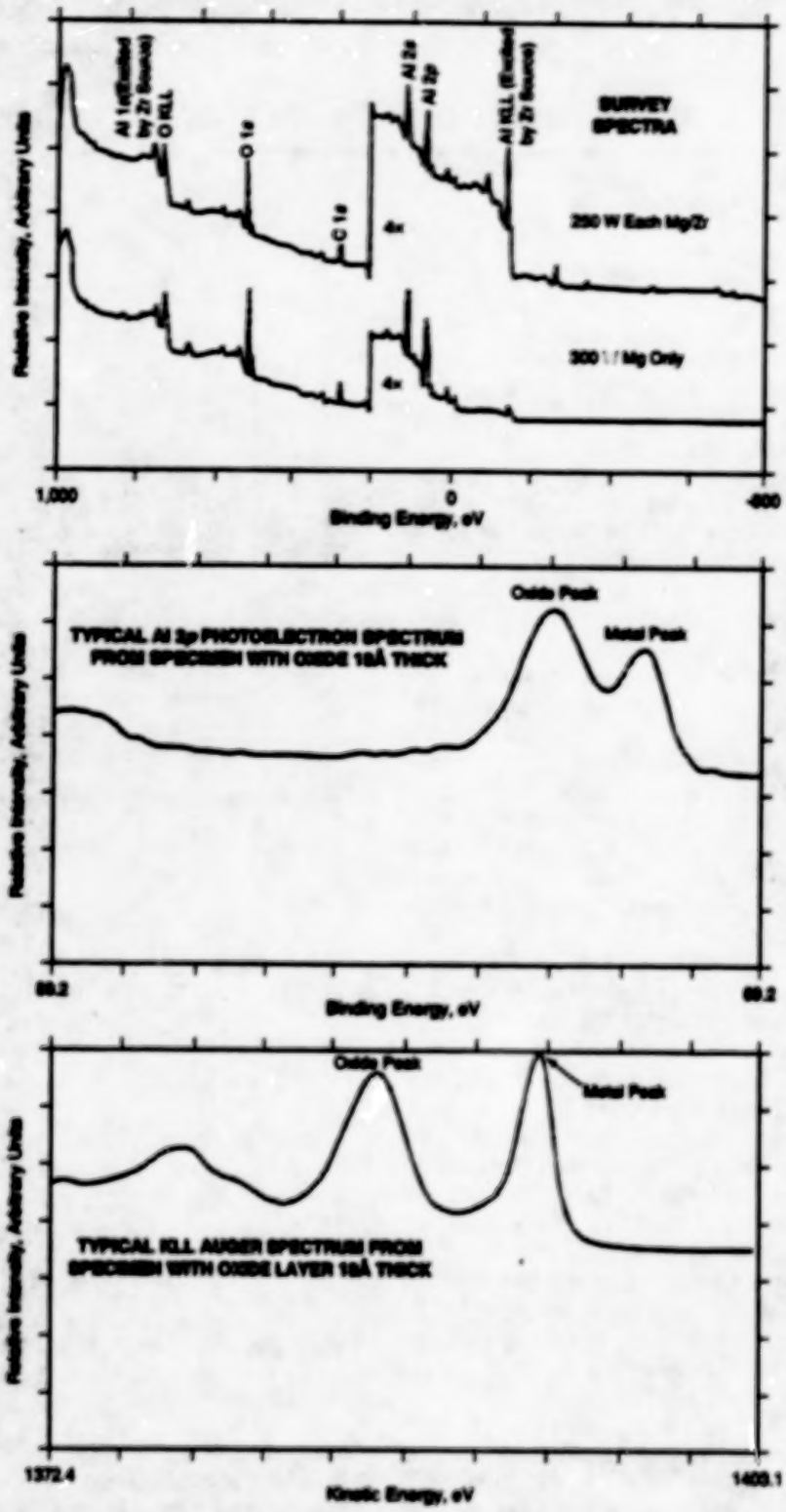

The XPS Spectra of the oxide-covered surface of a specimen of 2219 aluminum show the superiority of the improved (Mg/Zr) x-ray source over a conventional (Mg only) source. The improved source makes more Al KLL Auger electrons available, making possible the use of the KLL Auger metal and oxide peaks instead of (or in addition to) the Al 2*s* and 2*p* photoelectron peaks, the interpretation of which is more difficult and entails more subjectivity.

The improved source confers an additional benefit by making it possible to determine the depth of the oxide layer from the XPS measurements. The equation for the depth is

$$d = \lambda_o \sin(\theta)\, \ell_n\left(\frac{N_m \lambda_m I_o}{N_o \lambda_o I_m} + 1\right)$$

where d is the depth, I_o and I_m are the inelastic mean free paths of the KLL Auger transitions in the oxide and the metal, respectively; N_m and N_o are the volume densities (which are known properties) of the metal and oxide, respectively; and θ is the takeoff angle relative to the sample plane (this angle is a known parameter of the XPS apparatus).

This work was done by D. F. Allgeyer and E. H. Pratz of Martin Marietta Corp. for **Marshall Space Flight Center.** *Further information is contained in a TSP [see page 1].*
MFS-28631

Infrared Source for Testing Thermophotovoltaic Cells

An infrared band-pass filter is placed in front of flash lamps.

NASA's Jet Propulsion Laboratory, Pasadena, California

A source of pulsed infrared radiation for testing arrays of thermophotovoltaic cells has been obtained by placing an infrared band-pass filter in front of the large-area pulsed solar simulator (LAPSS) at NASA's Jet Propulsion Laboratory. The source provides infrared radiation within the required infrared spectral region, at the required intensity and approximate spatial uniformity, over a minimum area of 4 by 4 in. (10 by 10 cm).

This LAPSS, which has been described previously in *NASA Tech Briefs*, was originally designed to provide intense, pulsed radiation with a close approximation to the solar spectrum and nearly uniform intensity over an area large enough for testing arrays of photovoltaic cells. It includes two flash lamps, placed about 6 in. (about 15 cm) apart, that are pulsed for a period of 1.5 ms — long enough to measure the electrical characteristics of the cells but short enough to prevent significant heating of the cells.

The infrared band-pass filter for testing thermophotovoltaic cells is made by combining a blue/green band-pass glass absorption filter with a red/infrared band-pass glass absorption filter. The upper part of the figure shows the transmission spectrum of the combination filter. The lower part of the figure shows the estimated spectral irradiance of the filtered LAPSS radiation at a distance of about 7 in. (about 18 cm) from the flash bulbs, where the total irradiance of the unfiltered LAPSS is about 435 W/cm^2. The total irradiance of the filtered LAPSS radiation (that is, the spectral irradiance integrated over all wavelengths) is about 8 W/cm^2.

In a test, this source was used to illuminate an InGaAs thermophotovoltaic cell with 8 W/cm^2 of filtered infrared radiation. For comparison, the same thermophotovoltaic cell was illuminated with 7 W/cm^2 of radiation from a black-body source at a temperature of 1,200 °C. The output of the cell was considerably greater under the filtered infrared radiation than under the black-body radiation (short-circuit current almost three times as large); this confirms that the narrower filtered infrared spectrum is better matched to the spectral response of the cell than is the broad-spectrum black-body radiation.

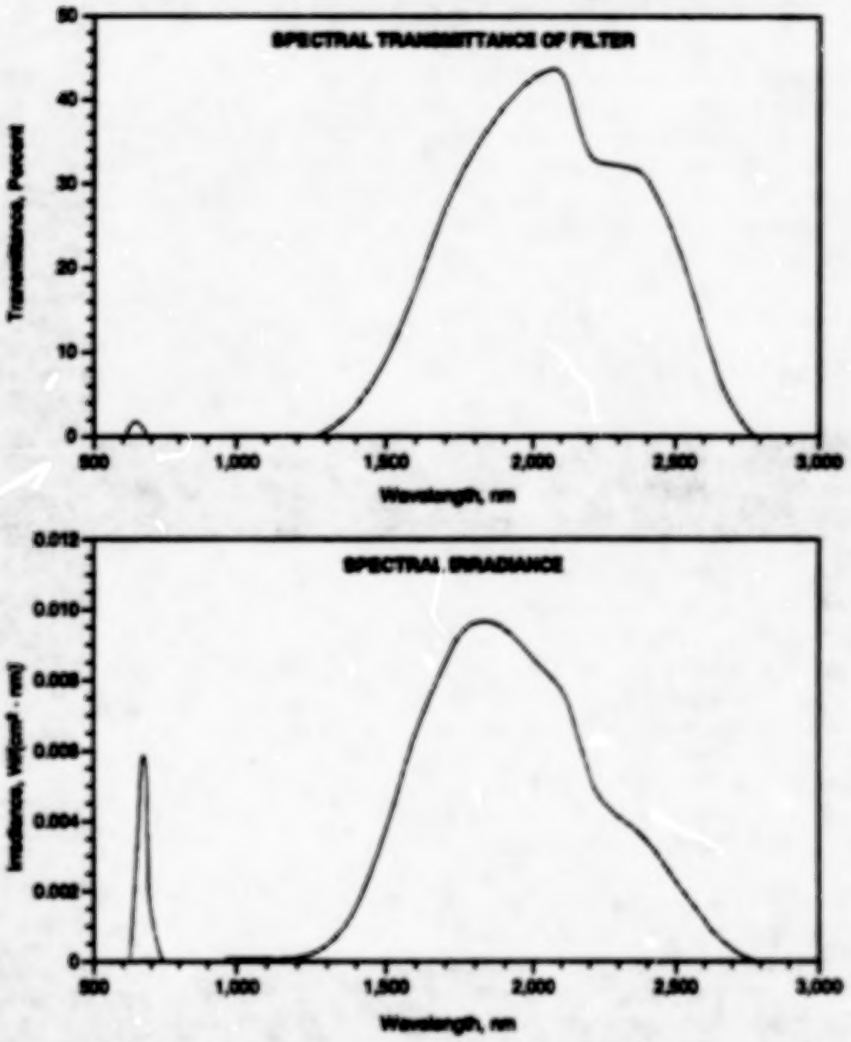

The Spectral Irradiance was computed by multiplying the spectral transmittance of the filter by a gray-body approximation of the LAPSS spectrum and by a correction factor. The peak in the spectral irradiance at 660 nm can be eliminated by replacing the red/infrared component of the filter with a black glass infrared filter.

This work was done by James J. Lin and Robert L. Mueller of Caltech for **NASA's Jet Propulsion Laboratory.** *Further information is contained in a TSP [see page 1].*
NPO-19493

Compact Color Schlieren Optical System

All of the lenses are stock items.

Lewis Research Center, Cleveland, Ohio

A compact, rugged optical system has been developed for use in rainbow schlieren deflectometry. The system features an unobscured telescope with a focal-length/aperture-width ratio of 30. It is made of carefully selected but relatively inexpensive parts.

Figure 1 shows a conventional gray-scale schlieren system. Light from a source is focused by a condensing lens on an aperture, which could be a pinhole or slit. Light diverging from this aperture is collected and collimated by a mirror and then passes through a test section, which contains a transparent medium, the spatial variations of the index of refraction of which are to be imaged and/or measured. (For example, if the medium is a fluid, the spatial variations in the index of refraction can be caused by gradients of temperature and/or density associated with flow of the medium.)

These spatial variations locally alter the phase of the optical wavefront (less precisely but more intuitively comprehensibly, they cause the light rays to bend). A decollimating mirror then forms a Fourier transform of the complex-amplitude transmittance of the medium in its back focal plane (makes the remaining collimated rays converge on a focal point, while it makes the bent rays strike the focal plane near, but not at, the focal point). A knife edge at or close to the focal point intercepts the amplitude and half of the phase information in the Fourier plane (the bent rays that strike the knife are prevented from reaching the camera). As a result, the image of the section projected into the camera is a pattern of light and dark areas that correspond to lateral (with respect to the line of sight) variations in the index of refraction of the medium.

A rainbow schlieren system differs from a gray-scale schlieren system in that the knife edge is replaced by either a color filter that changes linearly in hue from one side to the other or by one that changes radially in hue. A rainbow schlieren system offers sensitivity equal to that obtained with interferometry. It also offers the potential for quantification of the schlieren-image data, provided that the focal length of the optics and the relationship between the optics and the medium of interest in the test section are unambiguously known. Therefore, correction of astigmatism is desirable.

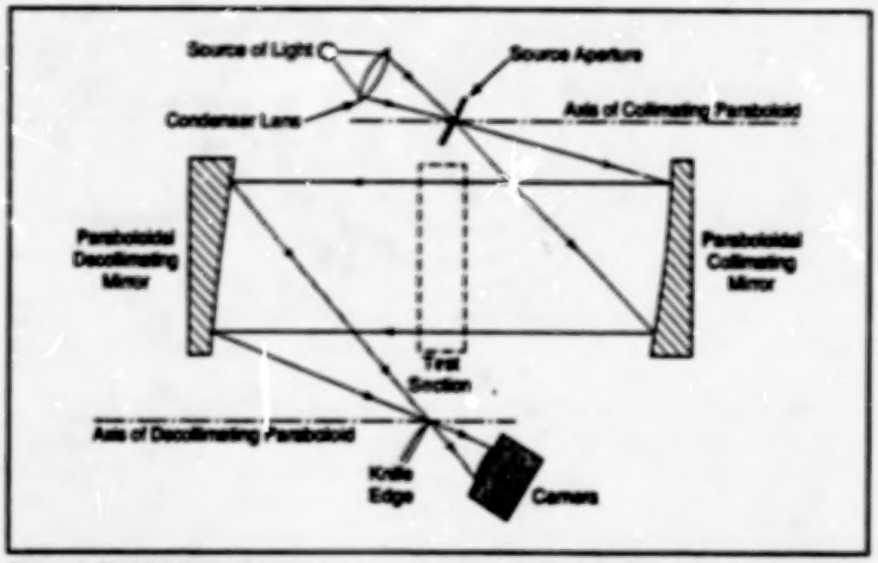

Figure 1. This Schlieren System has one of several common configurations of conventional gray-scale schlieren systems. In this case, the collimating and decollimating mirrors are off-axis-machined paraboloids.

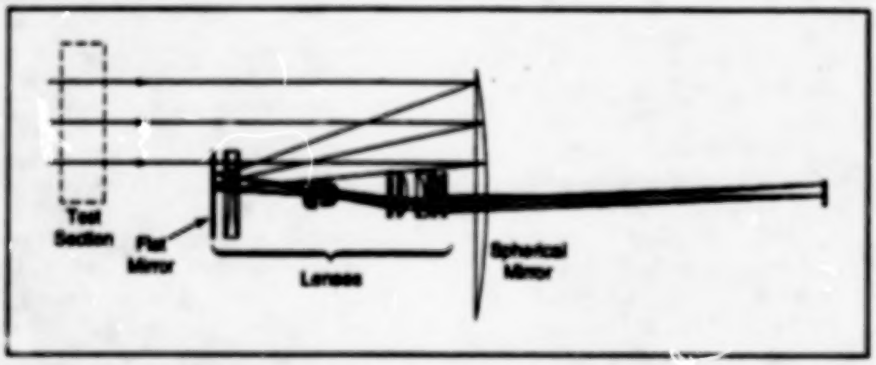

Figure 2. This Optical System is particularly well suited for use as a decollimating (as shown here) or as a collimating subsystem of a rainbow schlieren system.

Figure 2 shows the layout of the optical system that was developed for use in a rainbow schlieren system. More specifically, it shows an optical subsystem and a half length of the test section; this optical subsystem can be used for decollimation, and a similar optical subsystem at the other end of the test section can be used for collimation.

To minimize the cost, the design of the subsystem deliberately avoids aspherical lenses and off-axis-figured aspherical mirrors, which are expensive and difficult to make. The optics are nevertheless highly corrected by use of multiple carefully selected and carefully placed spherical reflecting and refracting optics: the subsystem is assembled from stock lenses, a spherical mirror, and a flat mirror.

An intentional by-product of the design is an optical system with loose tolerances on interlens spacing. One of the resulting advantages is insensitivity to errors in the fabrication of optomechanical mounts. Another advantage is the ability to compensate for some of the unit-to-unit variations inherent in stock lenses.

This work was done by Donald R. Buchele of ADF, Inc., and Delvon W. Griffin of Sverdrup Technology, Inc., for **Lewis Research Center**. *Further information is contained in a TSP (see page 1).*

LEW-15987

Multiple-Fiber-Optic Probe for Light-Scattering Measurements

Measurements can be taken over a range of scattering angles, without mechanical scanning.

Lewis Research Center, Cleveland, Ohio

A multiple-fiber-optic probe has been developed for use in measuring light scattered at various angles from specimens of materials. The probe was designed for both static and dynamic light-scattering measurements of colloidal dispersions. Light-scattering measurements can yield information on the structures and dynamics of the light-scattering media; in particular, such measurements are often used to determine distributions of sizes of particles suspended in liquids.

Heretofore, light scattered to various angles has been measured by use of conventional bulk optical components scanned mechanically with goniometers. Mechanical scanning of bulk optics is not well suited for static light-scattering measurements at low angles (such measurements are needed for determining molecular weights of polymers); it also does not provide simultaneous dynamic measurements of scattering at small intervals over a range of angles (such measurements are needed to determine particle-size distributions).

The multiple-fiber-optic probe is a compact, rugged unit that contains no moving parts and remains stationary during operation. Unlike most mechanically scanned bulk optic probes, this probe does not have to be restricted to operation in a controlled, research-laboratory environment. It can be positioned inside or outside a light-scattering chamber. It provides simultaneous measurements at small angular intervals over a range of angles, which can be made to include small scattering angles by merely orienting the probe in the appropriate direction. The probe (see figure) includes a bundle of optical fibers (11 fibers in the prototype) with their input ends arranged in a linear array at the back focal plane of a gradient-index-of-refraction (GRIN) lens.

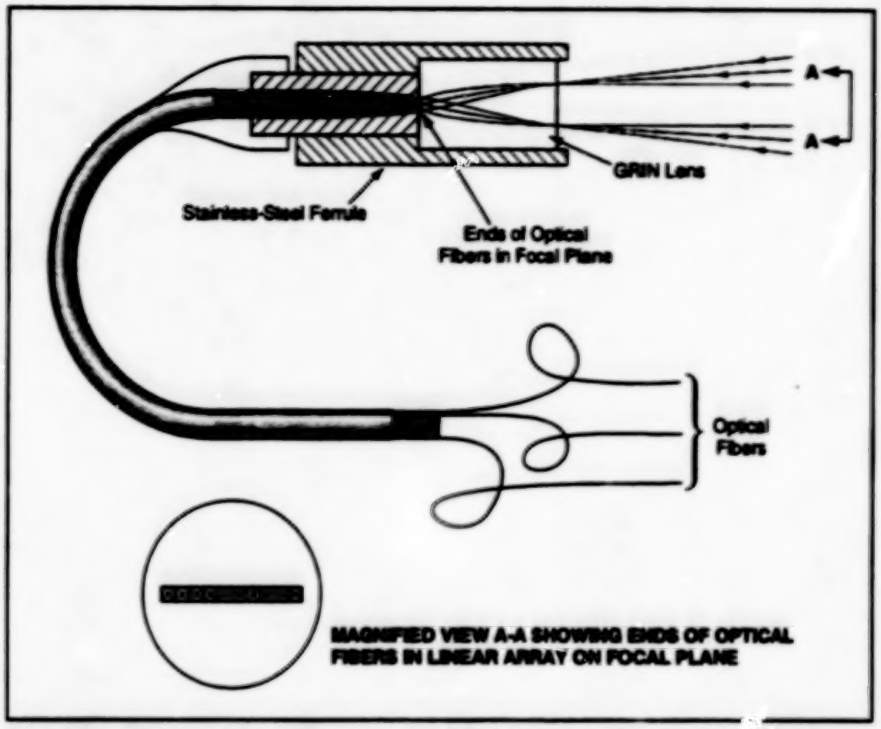
A
A
GRIN Lens
Stainless-Steel Ferrule
Ends of Optical Fibers in Focal Plane
Optical Fibers
MAGNIFIED VIEW A-A SHOWING ENDS OF OPTICAL FIBERS IN LINEAR ARRAY ON FOCAL PLANE

Each Fiber Gathers Light scattered into the GRIN lens at a different angle of incidence. Thus, the probe serves as a compact, rugged tool for simultaneously measuring light scattered at different angles, without need for mechanical scanning.

Light incident on the GRIN lens at a given angle is focused to a specific position on the focal plane. Thus, each optical fiber receives light scattered into an angular interval centered on an angle that depends on the position of the fiber along the linear array. The width of the angular interval and thus the uncertainty in the measurement angle is customarily expressed as the uncertainty in the direction cosine of the angle; this figure equals the ratio between the radius of the core of the optical fiber and the focal length of the GRIN lens.

The probe can be operated in a passive mode in which the light to be scattered is supplied by an external laser or other source. In that case, the output ends of all the optical fibers can be connected to photodetectors. Alternatively, one of the fibers can be used to carry light from a laser to the GRIN lens to illuminate the scattering medium, and the other fibers can then be used to measure the light back-scattered to various angles near 180°.

This work was done by Harbans Singh Dhadwal of the State University of New York and Rafat R. Ansari of Case Western Reserve University for **Lewis Research Center.** *Further information is contained in a TSP [see page 1].*
LEW-15460

Measuring High Temperatures in Ceramic-Fiber Blankets

Thermocouple wire is protected from an oxidizing atmosphere.

Ames Research Center, Moffett Field, California

Thermocouple assemblies have been devised specifically for measuring temperatures at fixed locations within insulating blankets made of such ceramic fibers as alumina, silicon carbide, and/or aluminoborosilicate. The thermocouples in these assemblies can measure temperatures from 100 to 3,200 °F (38 to 1,760 °C) in oxidizing atmospheres.

A thermocouple assembly of this type is L-shaped. It includes a type-R thermocouple — a platinum wire welded at the sensing tip to a wire of platinum alloyed with 13 percent rhodium. The wires are enclosed in an alumina sheath for protection against hot oxidation and mechanical damage (see figure).

Typically, the thermocouple assembly is installed in an insulating blanket to measure the temperature just inside one of the surface fabric layers. First, a flap is

cut to make a hole in the opposite fabric surface layer, then a slab of insulating core material is removed to make room for the thermocouple assembly. The assembly is inserted in the hole with the thermocouple wire leads trailing, and the sensing tip is placed in contact with the inner face of the desired surface layer. The assembly is bonded in place by use of ceramic cement. The slab of insulating core material is then reinserted, the flap is closed, and the edges of the flap are fastened in place by use of room-temperature-vulcanizing silicone-rubber cement. The thermocouple wires extending from the flap are then connected to the external circuitry that generates a temperature display from the thermocouple reading.

This work was done by Demetrius A. Kourtides of **Ames Research Center.** *Further information is contained in a TSP [see page 1].*

This invention has been patented by NASA (U.S. Patent No. 5,399,019). Inquiries concerning nonexclusive or exclusive license for its commercial development should be addressed to the Patent Counsel, Ames Research Center [see page 1]. Refer to ARC-11984.

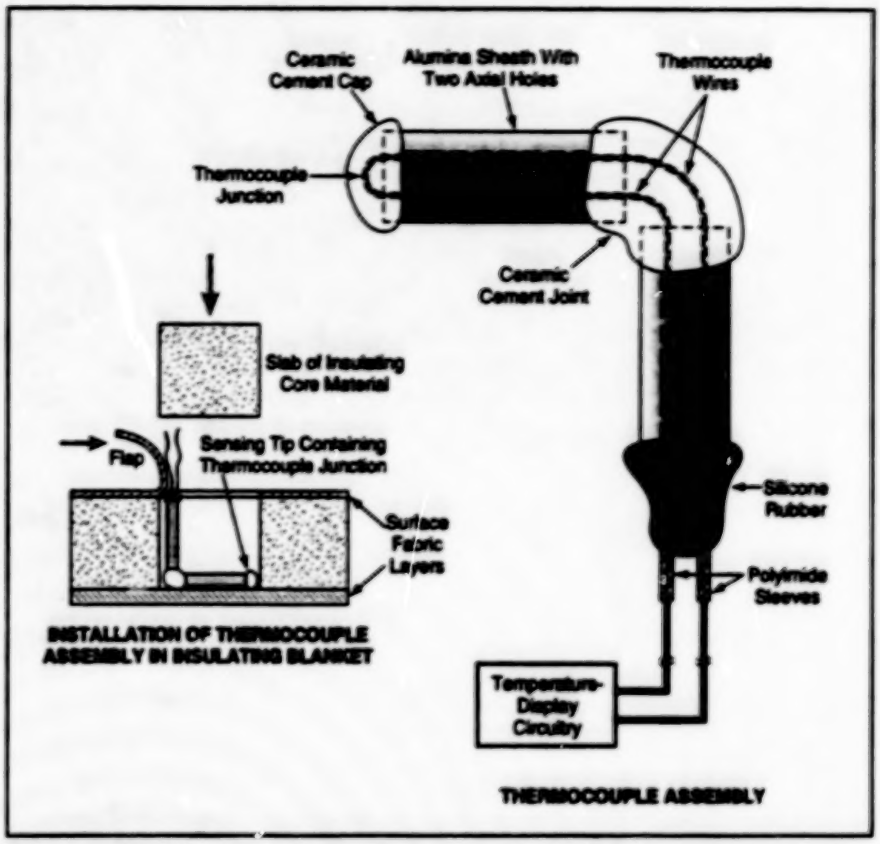

Refractory Materials protect and support the thermocouple wires in the hot measurement region.

Gamma-Ray Imager With High Spatial and Spectral Resolution

An externally segmented germanium detector is rotated in synchronism with a segmented aperture.

NASA's Jet Propulsion Laboratory, Pasadena, California

A γ-ray instrument has been developed to enable both (1) two-dimensional imaging at relatively high spatial resolution and (2) spectroscopy at a fractional-photon-energy resolution of about 10^{-3} in the photon-energy range from 10 keV to >10 MeV. In its spectroscopic aspect, the instrument enables identification of both narrow and weak γ-ray spectral peaks.

Heretofore, two-dimensional γ-ray imaging was possible, but only with relatively coarse energy resolution; a typical resolution would be 7 percent at a photon energy of 662 keV, and this is insufficient for spectroscopy of γ-ray spectral peaks and for detection of weak γ-ray spectral peaks. Prior to the development of the present instrument, it has not been possible to perform two-dimensional γ-ray imaging simultaneously with fine energy spectroscopy at photon energies above 10 keV.

The instrument (see figure) includes a large-volume germanium detector with an external electrode segmented into *N* distinct charge-collection regions (such detectors are manufactured with $5 \le N \le 12$). This detector is mounted in a cryostat and is used in conjunction with a segmented, linearly coded rectangular aperture that is placed between the detector and the γ-ray source. The widths of the detector segments equal those of the aperture segments, and the detector and aperture segments are aligned with

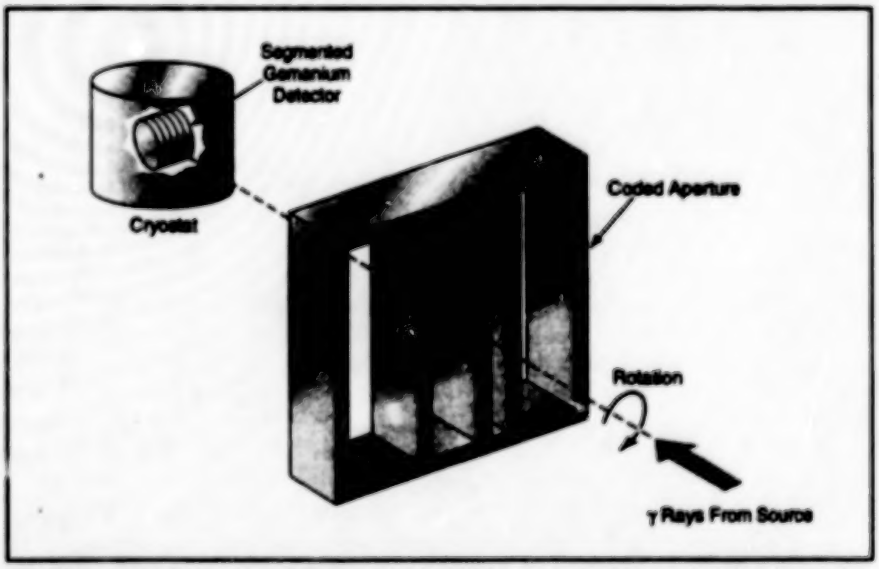

The Segmented Detector and Segmented Aperture are rotated in synchronism to acquire one-dimensional image data at a suitably large number of rotational positions. Deconvolution of these data yields a two-dimensional image.

each other, forming a one-dimensional imaging system.

To obtain data for two-dimensional imaging, the detector and aperture are rotated in synchronism (maintaining alignment) 180° about the line of sight, and detector readings are taken at multiple rotational positions along the way. The γ-ray image is then reconstructed by use of a computer to deconvolve the detector readings. Spatial resolution can be increased by increasing the distance between the aperture and the detector or by increasing the number of rotational positions where readings are taken. Both point and spatially extended γ-ray sources can be imaged. Large fields of view are possible if multiple detectors are used.

This work was done by John L. Callas, Larry S. Varnell, William A. Wheaton, and William A. Mahoney of Caltech for **NASA's Jet Propulsion Laboratory.** *Further information is contained in a TSP [see page 1].*
NPO-19140

Theory of Radiation-Induced Attenuation in Optical Fibers

An improved mathematical model accounts for the effects of dose rates.

NASA's Jet Propulsion Laboratory, Pasadena, California

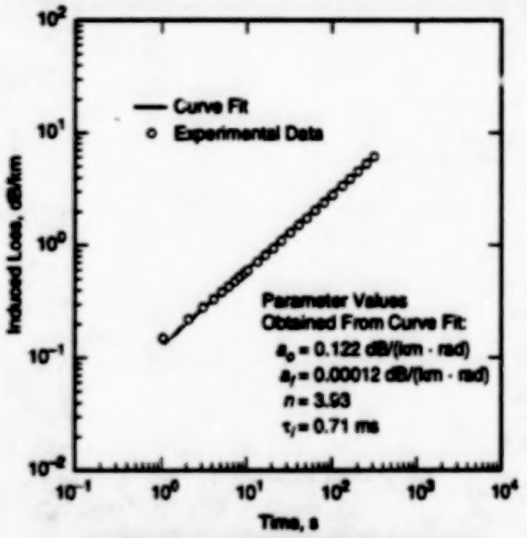

CURVE FIT TO CONSTANT-DOSE-RATE DATA

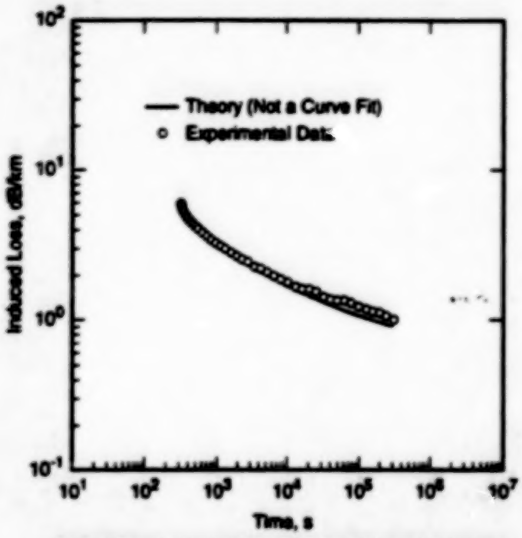

PREDICTED AND MEASURED RECOVERY CURVES

The Parameters Obtained in the Curve Fit were used to obtain a theoretical prediction of the recovery curve for comparison with the experimental recovery data.

An improved theory of radiation-induced attenuation of light in optical fibers accounts for the effects of dose rates. Previously, radiation-induced attenuation was represented by an empirical equation that does not account for dose rates; namely, $A = aD^b$, where A is the induced attenuation, D is the total dose of ionizing radiation, and a and b are constants. Accurate accounting for the effects of dose rates is necessary, for example, for extrapolating from high-dose-rate test data to predict the long-term performances of optical fibers that will be exposed to low dose rates in use.

The improved theory is based on kinetic aspects of the fundamental physics of color centers induced in optical fibers by radiation. The induced attenuation is proportional to the density of color centers, and part of this density decays by a thermal-annealing/recombination process after irradiation. Thus, once irradiation stops, there can be a partial recovery from the maximum induced attenuation.

The improved theory is based on a simple linear-superposition principle: the attenuation at any given time is considered to be the sum, over all time up to the present, of the attenuations induced in a sequence of infinitesimal and/or finite irradiation events, the attenuation from each event being modified by partial recovery since the time of that event. The partial-recovery effect can be incorporated into what amounts to a unit-impulse-response function, and the radiation impulse in each event can be represented as a stimulus proportional to the dose rate.

The equation that incorporates all of these effects is

$$A(t) = \int_0^t D'(t') \left\{ (a_0 - a_f)\left[1 + c_f(t - t')\right]^{\frac{-1}{n-1}} + a_f \right\} dt'$$

where $A(t)$ is the induced attenuation; t is time; $D'(t')$ is the time-dependent dose rate; a_0 is a coefficient that corresponds to the attenuation immediately after irradiation; a_f is a coefficient that corresponds to the final attenuation after long recovery; and $c = (1/\tau)(2^{n-1} - 1)$, where τ is the half-height lifetime of the recovery process and n is the material-dependent order of the recovery kinetics. The terms in braces constitute the unit-impulse-response function. The coefficients in this equation can be obtained by fitting the equation to experimental data. Then, the equation can be used to predict subsequent behavior under different conditions.

In an experimental test of the theory (see figure), a multimode optical fiber was bombarded by radiation from Co^{60} at a constant dose rate of 15.5 rad/s at a temperature of 21 °C and the induced attenuation was measured as a function of time. Then, the irradiation was stopped and the measurements continued. The

coefficients of the equation were obtained from a curve fit of the equation to the constant-dose-rate measurements, then the coefficients were inserted in the equation, which was used to calculate the post-irradiation recovery curve.

This work was done by Tsuen-Hsi Liu and Alan R. Johnston of Caltech for **NASA's Jet Propulsion Laboratory.** *Further information is contained in a TSP [see page 1].*
NPO-19334

Test-Aerosol Generator for Calibrating Particle Counters

Cheap, widely available medical nebulizers are used to generate the aerosols.

John F. Kennedy Space Center, Florida

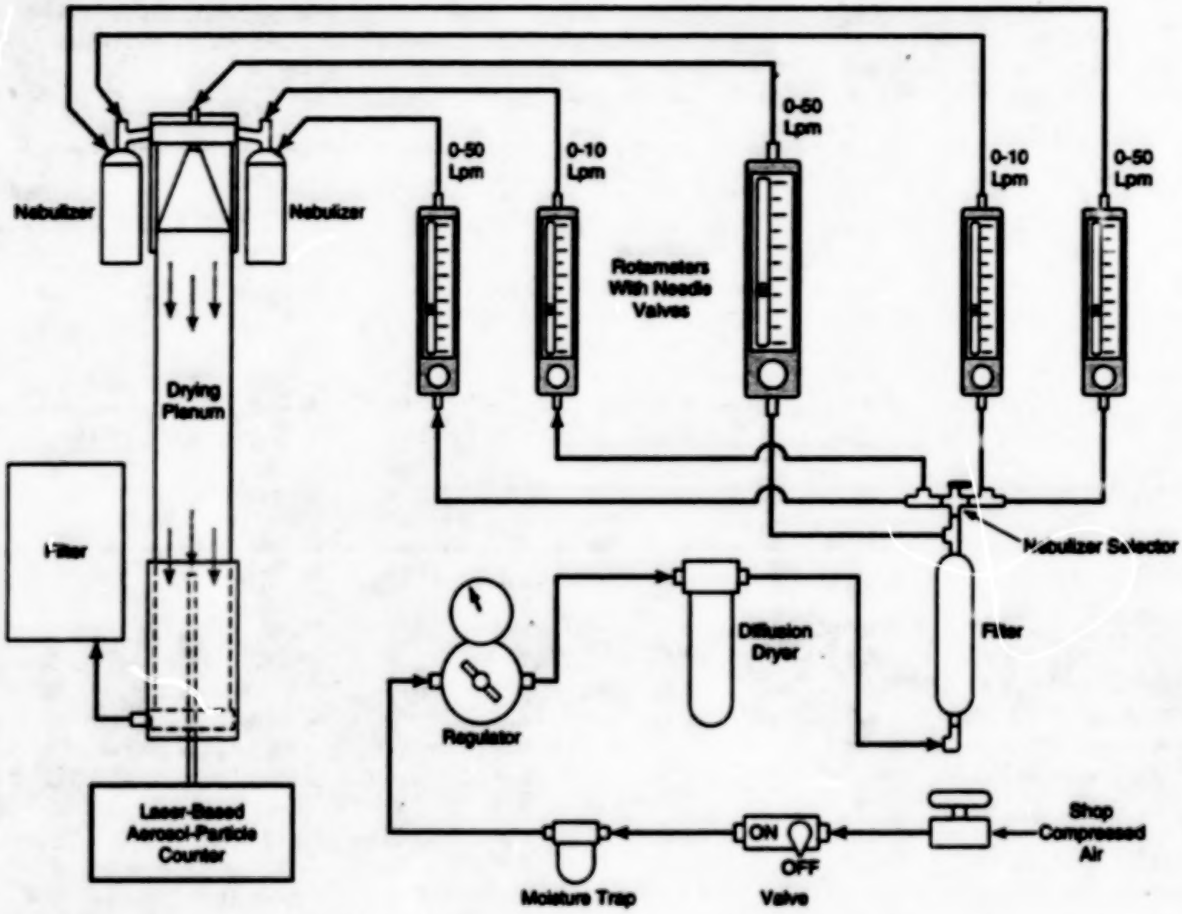

Valves and Flow Meters regulate flows of air to the drying plenum and the selected nebulizer. Because the size and concentration of particles suspended in the water in the nebulizers is known, accurate calibration of the particle counter is assured.

An apparatus generates a clean, stable aerosol stream for use in testing and calibrating a laser-based aerosol-particle counter. The size and concentration of the aerosol particles can be controlled to ensure accurate calibration.

The apparatus (see figure) includes two nebulizers mounted on top of a drying plenum in the form of a vertical cylinder. These are standard, cheap nebulizers of the type used for respiratory therapy. One of the nebulizers is selected for use in a given test or calibration run. Flows of air into the plenum and into the selected nebulizer are powered by compressed air (typically at a gauge pressure between 30 and 50 psi (207 and 345 kPa, respectively)) that has been filtered, dried, and regulated (typically to a gauge pressure between 10 and 15 psi (69 and 103 kPa, respectively)). Each of the two flows of filtered, regulated air to the selected nebulizer and the flow to the plenum is individually measured and controlled by use of a rotameter with a needle valve.

Each nebulizer includes a reservoir of water in which polystyrene latex spheres of the desired size (typically, a chosen diameter between 0.5 and 7 μm) have been suspended in the desired concentration. The nebulizer includes an atomizer. In the selected nebulizer, flowing air is mixed with the water/particle suspension to form a fog of droplets so small that they can remain suspended in air for a long time. This fog is the source of the desired aerosol.

As the fog descends along the vertical axis of the drying plenum, the water droplets evaporate and the flow of fog or aerosol becomes laminar, resulting in a laminar flow of polystyrene-latex-sphere aerosol at the bottom of the drying plenum. This flowing aerosol is sampled by use of an isokinetic-sampling tube, the outlet of which is connected to the aerosol-particle counter to be tested or calibrated.

This work was done by Paul A. Mogan of **Kennedy Space Center;** *Alois J. Adams of the University of Arkansas at Little Rock; Christian J. Schwindt, Timothy R. Hodge, and Tim J. Mallow of I-NET; and Anh A. Duong and Vyto V. Bukauskas of McDonnell Douglas Space & Defense Systems. Further information is contained in a TSP [see page 1].*
KSC-11701

Electrochemical Apparatus Simulates Corrosion in Crevices

A method of testing metal specimens for susceptibility to galvanic corrosion in crevices involves the use of a relatively simple electrochemical apparatus. By following this method, one can quantify the rates of corrosion of dissimilar-metal couples exposed to various etchants or other corrosive solutions. The apparatus includes a crevice cell, in which disk specimens of the metals of interest are mounted, separated by a polytetrafluoroethylene washer with radial channels that simulate crevices. The cell is filled with the corrosive solution of interest, which enters the channels. Galvanic currents are measured by electrically coupling the two metals together through a zero-resistance ammeter circuit. Rates of galvanic corrosion, which are proportional to galvanic currents, are measured and recorded for each metal couple. The apparatus was used to study the nickel/braze and braze/A286 stainless-steel couples as part of an investigation into the corrosion of nickel-plated A286 nozzle-coolant tubes in the main engine of the space shuttle. It was found that corrosion had been caused, in part, by acid etchants used during manufacturing of nozzles. The apparatus was also used to evaluate corrosion after treatment with corrosion inhibitors.

This work was done by S. Rachel Khoshbin, S. L. Jeanjaquet, and Jesse B. Lumsden of Rockwell International Corp. for **Marshall Space Flight Center**. *Further information is contained in a TSP [see page 1].*
MFS-30101

Ultrasonic-Transmission Testing Device

An ultrasonic-testing apparatus measures transmission through a component under inspection. The apparatus includes a hand-held ultrasonic transmitter that is placed on one side of the component and an ultrasonic receiver that is placed on the other side. However, there is no need to hold or manually align the receiving transducer after initial setup. The transmitter is loosely inserted in a magnetic assembly on one side, while the receiver is placed in another magnetic assembly on the other side. The magnetic coupling keeps the transmitter and receiver assemblies pressed against the component and keeps the receiver aligned with the transmitter as the transmitter is scanned across the surface of the component. The receiver can thus be moved to locations that might otherwise be inaccessible.

This work was done by Victor Ray Atkins and Carl Bouvier of Martin Marietta for **Marshall Space Flight Center**. *Further information is contained in a TSP [see page 1].*

Inquiries concerning rights for the commercial use of this invention should be addressed to the Patent Counsel, Marshall Space Flight Center [see page 1]. Refer to MFS-31007.

Apparatus To Test Solvent Stress Crazing of Polymer Sheets

An apparatus that is simple to make, operate, and maintain can be used to determine the abilities of transparent polymeric seal materials to resist stress crazing when exposed to various cleaning solvents. The apparatus includes pulleys, a cable, and weights to apply a constant tension to a specimen sheet immersed in the test fluid in a glass vessel. The specimen can be observed through the wall of the vessel at any time during the test. The level of applied tension is chosen to stress the specimen at a given percentage of the ultimate tensile strength of the specimen material. The specimen is observed at intervals to determine whether it has begun to craze, and the time for onset of crazing is plotted as a function of the applied stress. The test is terminated if no crazing is observed after 24 hours. The design of the apparatus provides for visual observation of the specimen at any time during the test and for ease of removal of fluid via a drain port at the bottom of the glass vessel.

This work was done by Gareth L. Simpson and William S. Hoult of Rockwell International Corp. for **Marshall Space Flight Center**. *Further information is contained in a TSP [see page 1].*
MFS-30075

Books and Reports

Water/Ice Heat Sink With Quick-Connect Couplings

A report consists of the main text of U. S. Patent 5,392,844, which presents additional detailed information on the apparatus described in "Direct-Interface, Fusible Heat Sink" (ARC-11920), *NASA Tech Briefs*, Vol. 16, No. 9 (September 1992), page 114. To recapitulate: the apparatus is a phase-change heat sink in which heat is dissipated by direct contact between water (the circulated cooling fluid) and ice (the phase-change heat-sink material). The heat sink includes an elastomeric bladder that contains the water/ice phase-change medium, through which the cooling water is circulated. The circulating water enters and leaves the interior of the bladder through two sets of identical quick-connect couplings that include female parts embedded in one wall of the bladder and male parts that are connected to the external plumbing. The female parts contain piston-type valves spring-loaded in the closed position; they are designed to prevent leakage when the male parts are removed, and to be pushed open by the mating male parts. The female parts are left in place when the heat sink is prepared for operation by freezing the water in the bladder. The design also provides for a bypass flow of water to melt ice that initially blocks the main flow passages in the female parts of the couplings when the apparatus is first put into operation. The report describes the entire apparatus, with special emphasis on those features of the quick-disconnect couplings that govern the flow of water under various operating conditions and plumbing configurations; these features are the subjects of the patent claims.

This work was done by Curtis Lomax and Bruce Webbon of **Ames Research Center**. *To obtain a copy of the report, "Quick Connect Coupling," see TSP's [page 1].*

This invention has been patented by NASA (U.S. Patent No. 5,392,844). Inquiries concerning nonexclusive or exclusive license for its commercial development should be addressed to the Patent Counsel, Ames Research Center [see page 1]. Refer to ARC-13374.

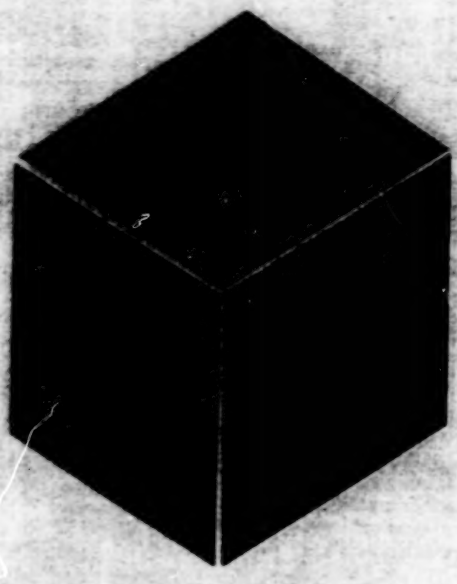

Materials

Hardware, Techniques, and Processes

35 Lightweight, Thermally Insulating Structural Panels
35 Coating Silicon-Based Ceramics With Durable Mullite
36 Extruded Self-Lubricating Solid for High-Temperature Use
37 Iridium Aluminide Coats for Protection Against Oxidation
37 Improved Synthesis of Potassium β″-Alumina
38 Advanced Polymer for Multilayer Insulating Blankets

BLANK PAGE

Lightweight, Thermally Insulating Structural Panels

Thermal conductivities are smaller than those of the best commercial insulating materials.

NASA's Jet Propulsion Laboratory, Pasadena, California

Lightweight, thermally insulating panels that also serve as structural members have been developed. In the original intended application, the panels would be used to house electronic circuitry aboard a vehicle that would explore the surface of Mars. On Earth, panels of this type would be especially suitable for use in low-air-pressure environments in which lightweight, compact, structurally supporting insulation is needed; for example, aboard high-altitude aircraft or in partially evacuated panels in refrigerators.

A panel of this type (see Figure 1) is a low-thermal-conductivity composite-material honeycomb-core/sandwich that affords thermal insulation over wide pressure and temperature ranges. The convective transfer of heat in an ordinary honeycomb core would be significant at pressures down to 1 torr (about 130 Pa). The core is filled with a silica aerogel. This filling eliminates the convective transfer of heat; it also exhibits very low thermal conductivity. Furthermore, this aerogel is opacified with 15-weight-percent Al particles smaller than 2 μm to minimize radiative heat transfer.

Thermal conduction through the thickness of the panel via the honeycomb walls is minimized by making the honeycomb walls as thin as possible (in this case, occupying only 3.4 percent of the cross-sectional area) while still providing

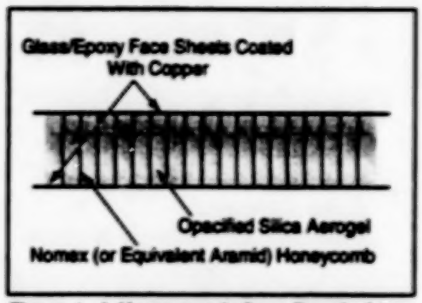

Figure 1. A Honeycomb-Core Panel of low thermal conductivity is filled with a low-thermal-conductivity, opacified silica aerogel that prevents convection and minimizes internal radiation. The copper coating on the face sheets reduces radiation.

adequate structural support. The honeycomb is made of Nomex (or equivalent aramid), which offers the required strength and rigidity, plus a thermal conductivity lower than that of other available composite-core materials. The face sheets are made of low-thermal-conductivity glass/epoxy composites. They are coated with copper to obtain low emissivity and thereby to further reduce transfer of heat by radiation.

The effective overall thermal conductivities of a panel of this type and several other types were measured at representative temperatures in a carbon dioxide atmosphere at a pressure of 10 torr (1.3 kPa). The results of some of these measurements are plotted in Figure 2, which shows clearly that the effective overall thermal conductivities of the developmental panels are smaller than those of state-of-the-art commercial non-structurally-supporting foam and fibrous insulations.

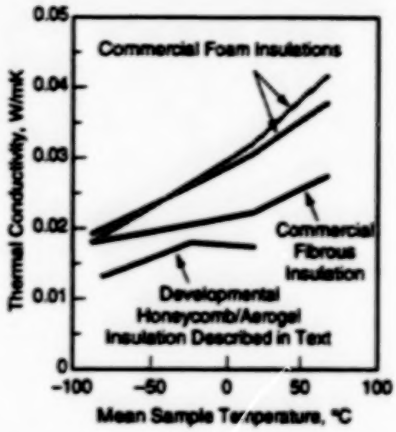

Figure 2. These Thermal Conductivities Were Measured in a 10-torr carbon dioxide atmosphere.

This work was done by Howard J. Eisen, Gregory Hickey, Liang-Chi Wen, William E. Layman, Richard A. Rainen, and Gajanana C. Birur of Caltech for **NASA's Jet Propulsion Laboratory**. *Further information is contained in a TSP [see page 1].*

NPO-19382

Coating Silicon-Based Ceramics With Durable Mullite

Elimination of the amorphous phase eliminates extensive cracking and debonding.

Lewis Research Center, Cleveland, Ohio

An improved plasma-spraying process deposits mullite (aluminum silicate) on silicon carbide substrates. The process is also expected to be useful in depositing mullite on substrates made of other silicon-based ceramics (e.g., Si_3N_4 and SiC/Si_3N_4 composites) and other ceramic substrates (e.g., AlN) that have coefficients of thermal expansion similar to those of mullite.

Mullite coats are highly desirable for silicon-based ceramic structural components of heat exchangers, gas turbine engines, and advanced internal-combustion engines. Mullite exhibits high chemical stability, low thermal conductivity, and a coefficient of thermal expansion approximately equal to those of silicon-based ceramics. Therefore, an adherent coat of mullite could serve as both a chemical and a thermal barrier that would protect the underlying ceramic against high-temperature chemical attack. In addition, overlayers of such other refractory oxides as alumina, yttria-based zirconia, or yttria could be applied to the base coats of mullite.

Until now, plasma-sprayed mullite coats have cracked and flaked away from substrates during thermal cycling, thereby losing their protective qualities. This cracking and debonding was found to be a consequence of the large proportion of amorphous (noncrystalline) mullite that formed during plasma deposition on cold substrates: during subsequent thermal cycling, the amorphous material crystallized when it was heated to temperatures above 1,000 °C. The newly crystallized material shrank, giving rise to cracks.

The improved process prevents the formation of amorphous mullite by maintaining high temperature of the sprayed deposit to allow crystallization to occur. For this purpose, the plasma spraying of mullite is done in a furnace that heats the substrate to about 1,000 °C. Once the substrate has reached the desired temperature, mullite powder is introduced into an argon-40-percent-helium plasma in a stream of argon gas. The deposited mullite adheres to the substrate and exhibits little or no cracking during thermal cycling (see figure). Tests have shown that mullite coats deposited by the improved process adhere and provide substantially greater

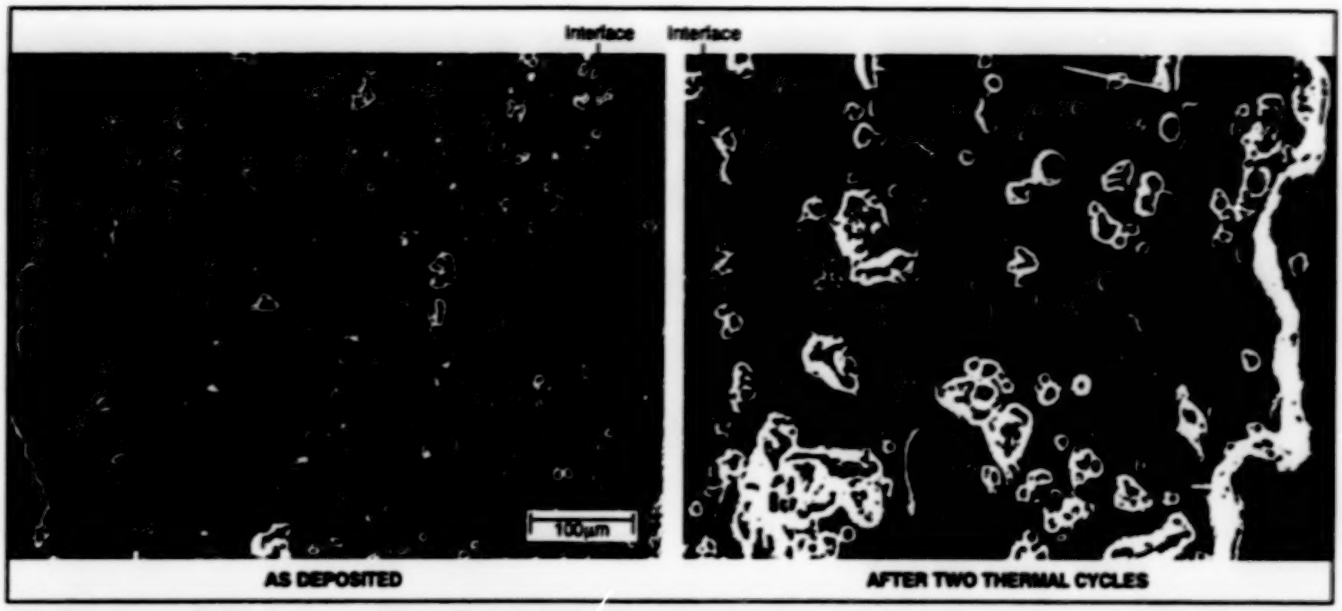

This Specimen of Mullite Coat on a Silicon Carbide Substrate contained no interconnected cracks and could thus protect the substrate against chemical attack, even after two thermal cycles. In each cycle, the specimen was suddenly heated to 1,000 °C, kept at that temperature for 24 h, and quenched in air to room temperature.

resistance to oxidation in dry air and corrosion by molten salt.

This work was done by Robert A. Miller and Nathan S. Jacobson of **Lewis Research Center** *and Kang N. Lee of Cleveland State University. Further information is contained in a TSP [see page 1].*

This invention has been patented by NASA (U.S. Patent No. 5,391,404). Inquiries concerning nonexclusive or exclusive license for its commercial development should be addressed to the Patent Counsel, Lewis Research Center [see page 1]. Refer to LEW-15561.

Extruded Self-Lubricating Solid for High-Temperature Use

Properties equal or exceed those of a powder-metallurgy version of this material.

Lewis Research Center, Cleveland, Ohio

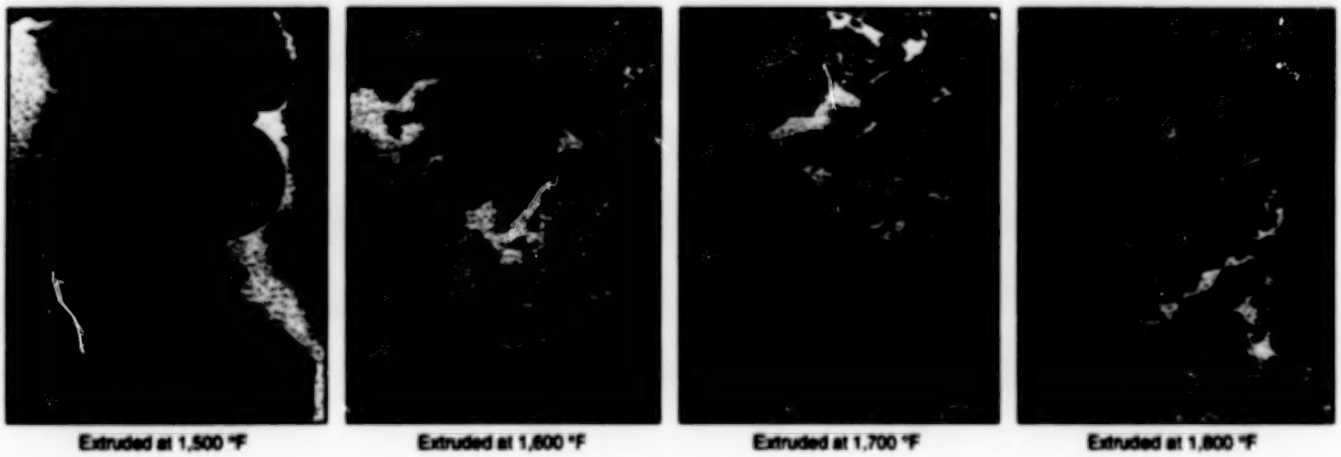

These Magnified Views of Etched Specimens of EX-212 all show porosity. Note that the pores are smallest in the specimen extruded at the highest temperature.

"EX-212" denotes a high-density extruded form of a composite solid material that is self-lubricating over a wide range of temperatures. The material has been developed for use in advanced engines at high temperatures at which ordinary lubricants are destroyed. An older form of the material, made by plasma spraying, is called "PS-212"; another older form of the material, made by powder metallurgy, is called "PM-212." All three forms of the material have the same chemical composition: they are made from powders of chromium carbide with a nickel-based binder (70 percent) combined with silver (15 percent) and with a eutectic mixture of barium and calcium fluorides (15 percent).

EX-212 was added to the "212" product line in an effort to enhance its commercial potential. Experiments were conducted to investigate the properties of "212" extruded at various temperatures. PS-212 powder for use in the extrusion experiments was prepared by blending the constituent powders. Then the powder was extruded into bars, at an area-

reduction ratio of 16:1, at temperatures of 1,400 °F (760 °C), 1,500 °F (816 °C), 1,600 °F (871 °C), 1,700 °F (927 °C), and 1,800 °F (982 °C). Measurements of frictional and strength properties of the bars indicated that the tribological and other physical properties of EX-212 equal or exceed those of PM-212. Overall results of the experiments indicated that extrusion temperatures are not critical for densification, but other properties depend on extrusion temperatures.

X-ray images of the bars showed relatively uniform, continuous extrusions with no bursts or discontinuities. Specimens made from the bars were inspected further by use of x rays and surface fluorescence and found to be generally porous. The amount of porosity was greatest in the bars extruded at lower temperatures and least in the bars extruded at the maximum temperature of 1,800 °F (982 °C).

Specimens made from the bars were subjected to tensile tests at room temperature, 800 °F (427 °C), 1,200 °F (649 °C), 1,400 °F (760 °C), and 1,600 °F (871 °C). For the most part, tests consisted of measurements of ultimate tensile strengths in a controlled-strain-rate testing machine. Generally, the bars extruded at lower temperatures exhibited greater tensile strengths at test temperatures from ambient to 1,200 °F (649 °C), whereas the bars extruded at higher temperatures exhibited greater strengths at 1,400 °F (760 °C), and 1,600 °F (871 °C). In all cases, elongation was less than 3 percent. The bars extruded at the lower temperatures exhibited the least ductility as measured in terms of tensile elongation. These test data were presented at the "Technology 2002" conference and exhibition.

This work was done by H. E. Sliney of **Lewis Research Center**, *W. J. Waters of Sverdrup Technology, Inc., R. F. Soltis of Omni, Inc., and K. Bernis of Case Western Reserve University. Further information is contained in a TSP [see page 1].*
LEW-15936

Iridium Aluminide Coats for Protection Against Oxidation

Iridium aluminide protects as well as platinum does at temperatures up to 1,600 °C.

Lewis Research Center, Cleveland, Ohio

Iridium aluminide coats have been investigated for use in protecting some metallic substrates against oxidation at high temperatures. The investigation was prompted by the need for cost-effective anti-oxidation coats for the walls of combustion chambers in rocket engines. Iridium aluminide coats may also prove useful in special terrestrial applications like laboratory combustion chambers and some chemical-processing chambers.

In the investigation, an iridium aluminide coat was formed by chemical vapor deposition from iridium carbonyl and tri-isobutyl aluminum precursors. The substrate was a water-cooled part of a center body for use in a cylindrical thrust chamber. Metallographic analysis showed the coat to be a dense mixture of iridium/aluminum compounds and elemental iridium.

The coated substrate was tested by subjecting it to simulated thruster-firing cycles in which the temperature at the interface between the coat and the substrate reached various peak values from 430 to 2,000 °C. At 2,000 °C, the iridium aluminide coat was found to be as protective as a pure iridium coat. At temperatures up to about 1,600 °C, the iridium aluminide coat was found to be as protective as a platinum coat; that is, the rate of oxidation with the iridium aluminide coat was found to be the same as that with a platinum coat — of the order of a hundredth the rate of oxidation with a pure iridium coat.

Not only does iridium aluminide provide superior protection against oxidation, it also costs about half as much as iridium and platinum do. In addition, iridium aluminide protects against oxidation at temperatures equal to or greater than those for pure iridium. Iridium aluminide may not be suitable for use on some substrates; for example, at temperatures near and above 2,000 °C, low-melting-temperature iridium/niobium compounds can form, with resultant degradation of both coats and substrates. It may be necessary to use intermediate diffusion-barrier coats in such cases. Further investigation will be necessary to understand process kinetics and optimize process parameters.

This work was done by Richard B. Kaplan, Robert H. Tuffias, Raffaele La Ferla, and Qin Jang of Ultramet for **Lewis Research Center**. *Further information is contained in a TSP [see page 1].*
LEW-15645

Improved Synthesis of Potassium ß″-Alumina

The ß″ phase can be synthesized from alternative formulations.

NASA's Jet Propulsion Laboratory, Pasadena, California

Improved formulations of precursor materials have made it possible to synthesize nearly-phase-pure potassium ß″-alumina solid electrolyte (K-BASE) powder. The precursor materials in question are microhomogeneous powders (or, alternatively, gels) that contain K^+, Mg^{2+}, and Al^{3+}. Conversion of these materials to K-BASE is effected by heating them in air at temperatures between 1,373 and 1,773 K. K-BASE powder thus produced can be used in potassium-working-fluid alkali-metal thermal-to-electric conversion (K-AMTEC), in which the heat-input and heat-rejection temperatures are lower than those of sodium-working-fluid AMTEC (Na-AMTEC). An additional potential use lies in the purification of potassium by removal of sodium and calcium.

High-quality potassium ß″-alumina powder is necessary for making high-quality potassium ß″-alumina ceramics needed in K-AMTEC cells. Difficulties were encountered in previous attempts to synthesize potassium ß″-alumina by direct solid-state chemical reactions among oxides because the temperatures needed for formation of the ß″-alumina phase are high enough to cause escape of K_2O and thus loss of potassium from the ß″-alumina. Liquid-phase synthesis has also proven difficult

because it involves still higher temperatures at which the β″ phase is crystallographically unstable.

One class of improved precursor materials comprises gels made by hydrolysis of solutions of alkoxides of K^+, Mg^{2+}, and Al^{3+}; isopropoxides, ethoxides, *t*-butoxides, and *n*-butoxides have been used. An alternative class of precursor materials comprises polymeric oxalate salts of the three metals in the appropriate ratios. Mg^{2+} ions are included in the formulations because they stabilize the β″ phase. (Prior to the development of these precursor materials, stabilizing ions were not included.) In experiments, the improved precursor materials were fired at temperatures from 1,373 K to 1,773 K to obtain crystalline potassium β″-alumina.

This work was done by Roger M. Williams, Barbara Jeffries-Nakamura, Margaret A. Ryan, Dennis E. O'Connor, Adam Kisor, and Mark Underwood of Caltech for **NASA's Jet Propulsion Laboratory**. *Further information is contained in a TSP [see page 1].*
NPO-19210

Advanced Polymer for Multilayer Insulating Blankets

This polymer resists degradation by monatomic oxygen.

Marshall Space Flight Center, Alabama

A polymer that resists degradation by monatomic oxygen has been invented by scientists at NASA and is undergoing commercial development under the trade name "Acrimide" (which stands for "atomic-oxygen-resistant imidazole"). Originally, this polymer was intended for use in thermal blankets for spacecraft in low orbit around the Earth, where degradation by monatomic oxygen limits the useful lifetimes of polymeric materials. If this polymer proves equally stable in terrestrial environments, then it might prove useful on Earth in outdoor applications in which sunlight and ozone degrade other plastics.

Acrimide can be used, for example, to make threads and to make films coated with metals for reflectivity. In preliminary experiments, film specimens of Acrimide with silver/nickel-alloy mirror coats were found to resist attack by atomic oxygen and to exhibit thermal-blanket performance comparable to that of Kapton (or equivalent) polyimide coated with aluminum.

This work was done by R. Ross Haghighat and Allan Shepp of Triton Systems, Inc., for **Marshall Space Flight Center**. *Further information is contained in a TSP [see page 1].*

Inquiries concerning rights for the commercial use of this invention should be addressed to the Patent Counsel, Marshall Space Flight Center [see page 1]. Refer to MFS-26335.

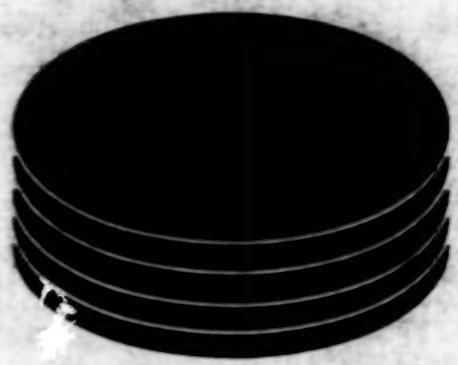

Computer Programs

Phisical Sciences

41 Software for Generation of ASTER Data Products

Fabrication Technology

41 Another Program Simulates a Modular Manufacturing System

BLANK PAGE

These programs may be obtained from COSMIC. Please contact

COSMIC®
Computer Services Annex
University of Georgia
Athens, GA 30602
Telephone No. (404) 542-3265

Physical Sciences

Software for Generation of ASTER Data Products

Software that functions in the EOSDIS computing environment has been developed to generate data products from the Advanced Spaceborne Thermal Emission and Reflection Radiometer (ASTER). This software processes high-resolution image data from (a) visible and near infrared (VNIR), (b) short-wavelength infrared (SWIR), and (c) thermal infrared (TIR) radiometric readings to generate data on radiative and thermal properties of the atmosphere and surface of the Earth. The data products include the following:

- Brightness temperature at a horizontal resolution of 90 m;
- Surface reflectances and surface radiances in the VNIR band at a horizontal resolution of 15 m and in the SWIR band at a horizontal resolution of 30 m;
- Surface reflectance in the TIR band at a horizontal resolution of 90 m;
- Surface emissivity (over land only) at a horizontal resolution of 90 m;
- Land surface temperature at a horizontal resolution of 90 m;
- A polar classification map showing water, wet ice and slush, snow and ice, land, shadow, water cloud, and ice cloud, with resolutions of 15, 30, and 90 m; and
- Topographical information from along-track stereoscopic observations in the near infrared band.

This work was done by Alexander T. Murray, Bjorn T. Eng, and Charles C. Vogel of Caltech for **NASA's Jet Propulsion Laboratory**. *Further information is contained in a TSP [see page 1].*
NPO-19701

Fabrication Technology

Another Program Simulates a Modular Manufacturing System

The system can consist of a production line with as many as 18 stations in series.

SSE5 is a computer program that provides a simulation environment for modeling manufacturing systems that contain relatively small numbers of stations and operators. Although SSE5 was designed to simulate manufacturing of apparel, it could be used in other manufacturing domains.

The SSE5 simulation software package is most valuable for small or medium-size firms, including those that lack the expertise to develop detailed mathematical models or have only minimal knowledge in describing manufacturing systems and in analyzing the results of simulations on mathematical models. The user does not need to know a simulation language to use SSE5. SSE5 has been used by a number of apparel-manufacturing firms to design new manufacturing modules and to evaluate existing modules. SSE5 is one of a suite of programs that simulate small manufacturing systems. Two other programs, SSE3 and SSE6, are also available from COSMIC, bundled together as SSE (MFS-26245). Each program models a slightly different manufacturing scenario.

SSE5 can be used to design and evaluate a modular manufacturing system with one line and a maximum of 18 stations in a series. Each station can include a maximum of eight machines performing identical operations in parallel. A maximum of 26 operators, of variable efficiency, is allowed. Some operators are assumed to be cross-trained and able to work at any station at varying efficiency and some are fixed at a single station. The model incorporates the assumption that unlimited space is available for work in process in front of each station. There must always be enough items in front of the first station to prevent a delay while waiting for an item. Work is done in lots; a lot can consist of one or many items. SSE5 also incorporates the assumption that there are no machine breakdowns.

SSE5 is written in Turbo C v2.0 for IBM PC-series and compatible computers running MS-DOS and has been successfully compiled using Turbo C++ v3.0. Sample MS-DOS executable codes and sample input/output files are included on the distribution medium. The program requires a VGA graphics display and at least 128K of random-access memory for execution. The standard distribution medium for SSE5 is a 3.5-in. (8.89-cm), 1.44MB, MS-DOS format diskette. SSE5 was developed in 1993.

This program was written by Burnard J. Schroer and Jian Wang of the University of Alabama in Huntsville for **Marshall Space Flight Center**. *Further information is contained in a TSP [see page 1].*

Inquiries concerning rights for the commercial use of this invention should be addressed to the Patent Counsel, Marshall Space Flight Center [see page 1]. Refer to MFS-26284.

BLANK PAGE

Mechanics

Hardware, Techniques, and Processes

45 Soft Wire Seals for High Temperatures and Pressures
45 Processing Laser-Velocimeter Measurements From a Turbopump
46 Rotary Release Mechanism With Fusible Link
47 Cross Coupling Between Attenuators in a Docking Mechanism
48 Mathematical Modeling for Control of a Flexible Manipulator
49 Dual-Eccentric Clevis Joint

BLANK PAGE

Soft Wire Seals for High Temperatures and Pressures

These seals can be fabricated easily, at relatively low cost.

NASA's Jet Propulsion Laboratory, Pasadena, California

Soft metal wires can be used to make O-ring and similar seals for vessels, flanges, and fittings subject to pressures ≥1,000 psi (≥7 MPa) and temperatures ≥100 °C. Heretofore, seals for such high-pressure, high-temperature applications have been fabricated by precise machining of mating surfaces and have therefore been expensive; the prices of some commercial seals for these applications are as high as $6,500. The seals containing soft metal wires can be made inexpensively because they can be fabricated to looser tolerances like those of lower-temperature, lower-pressure elastomeric-O-ring seals, which they resemble.

The figure illustrates a laboratory pressure vessel with a soft wire seal. In fabrication of this vessel, matching sealing grooves are machined into a flange on the main body of the vessel and in a cap that is bolted onto the flange. The wire used as the O-ring seal is made of 1100 aluminum, which is relatively soft. The diameter of the wire is chosen so that the cross-sectional area of the wire exceeds the combined cross-sectional areas of the grooves: this is necessary to make excess wire material available to be squeezed out of the grooves to form a seal.

The wire is cut to the circumference of the groove, then the ends of the wire are fused together to form the sealing ring. The ring is laid in the sealing groove on the flange. Then the cap is laid over the sealing ring and bolted onto the flange, thereby squeezing the wire material both into the grooves and across adjacent areas of the flange and cap, forming a seal.

Seals of this type can also be made with noncircular grooves and with soft metals other than aluminum. For example, gold would perform well, though of course it would be expensive. For other applications, silver would be a good choice.

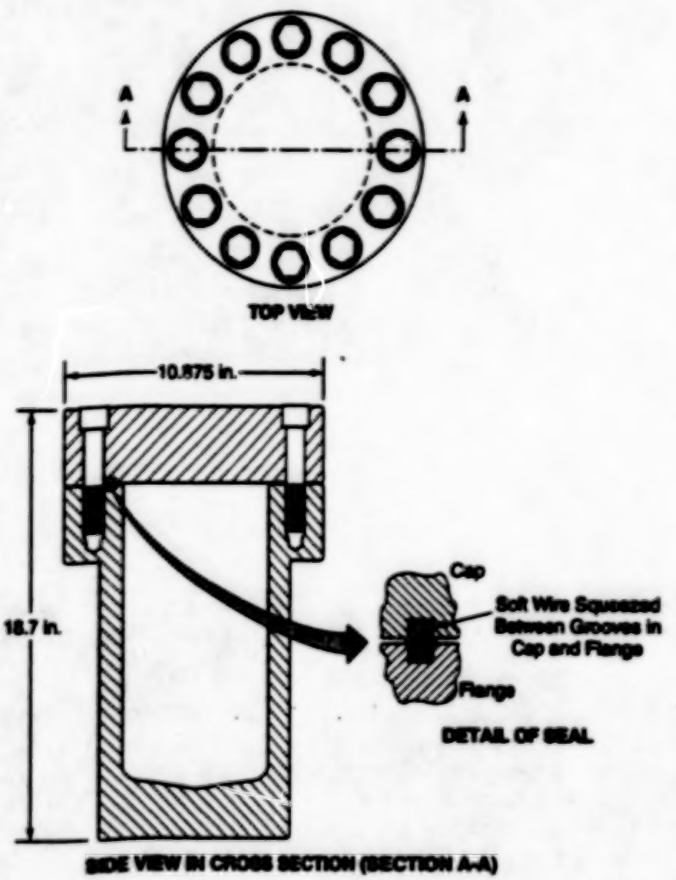

Soft Metal (Aluminum) Wire in Grooves forms a high-temperature, high-pressure seal between the cap and the flange.

This work was done by Peter Tsou of Caltech for **NASA's Jet Propulsion Laboratory.** *Further information is contained in a TSP [see page 1].*
NPO-19141

Processing Laser-Velocimeter Measurements From a Turbopump

A program computes circumferentially averaged velocities, total pressures, and other flow quantities.

Marshall Space Flight Center, Alabama

The Laser Velocimeter Axial Plane Data Reduction computer program computes flow velocities and related flow quantities from laser-velocimeter measurements in a turbopump. This program replaces an older, less accurate program that required tedious manipulation of data to perform simple analyses.

The measurements are taken on radial laser-velocimeter lines of sight at 144 points in each of two planes perpendicular to the axis; one plane immediately upstream and one plane immediately downstream of a four-blade inducer. The measurement points in each plane are located at 9 equal radial intervals between the hub and the tips of the inducer blades, and at 16 equal angular intervals that together span the 90° interval between corresponding points on adjacent inducer blades (see figure). Thus, the measurements in each plane provide for characterization of the velocity field at 144 points distributed evenly in one complete blade-to-blade passage; by use of circumferential averaging under an assumption of symmetry, the measurements thus enable characterization of velocities throughout the plane.

The output of the laser velocimeter is, in effect, a set of data on the magnitude and direction of the velocity vector at each measurement point. As part of the effort to understand the flow field, it is necessary to determine velocities in circumferentially averaged form; that is, to

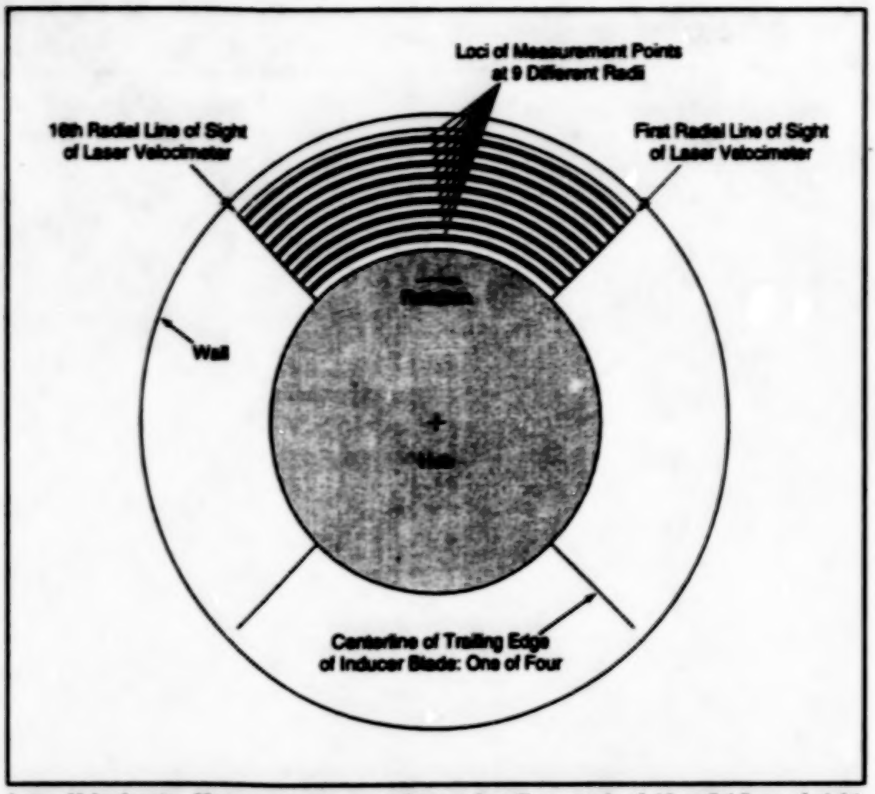
Loci of Measurement Points at 9 Different Radii
16th Radial Line of Sight of Laser Velocimeter
First Radial Line of Sight of Laser Velocimeter
Wall
Centerline of Trailing Edge of Inducer Blade: One of Four

Laser-Velocimeter Measurements are taken at 9 radii on each of 16 radial lines of sight spaced equally around a 90° sector of each measurement plane.

determine the components of velocities as functions of radius, independent of circumferential position. It is also necessary to verify the laser-velocimeter output data by comparison between rates of flow calculated from these data and rates of flow measured by independent means.

The program separates the velocity measured at each point into its components. An area-averaged axial velocity is calculated from the pointwise data by performing a spline integration over the 90°, hub-to-wall span. The circumferential and axial components of velocity are mass-averaged over the span under an assumption of constant density.

Inasmuch as no measurements are taken near the wall, calculation of the volumetric flow rate necessitates extrapolation of velocity to the wall. For this purpose, the inlet flow is assumed to be fully developed turbulent pipe flow with a speed v given by $v = V(y/R)^{1/n}$, where V is the maximum speed at the center line of the pipe, y is the distance from the wall, R is the radius from the center line to the wall, and n is a function of the Reynolds number of the flow and is determined by the user. V can be calculated from n, R, and the rate of flow measured by independent means.

Having calculated the circumferentially averaged velocities, the program calculates the spatial distribution of total pressure from these velocities plus a measurement of total pressure at one point in the plane of the laser-velocimeter data. The program does this by solving a differential equation for the total pressure as a function of the radius and the local velocity components. The equation was derived from (1) Euler's equation for the conservation of radial momentum in steady-state, axisymmetric flow of an inviscid fluid with no external forces and no radial component of velocity and (2) Bernoulli's equation for conservation of energy in the same flow. Finally, the program calculates the spatial distribution of efficiency by use of the Euler efficiency equation.

This work was done by San Y. Meng, Kevin J. Lunde, and Gerald A. Lee of Rockwell International Corp. for **Marshall Space Flight Center**. *Further information is contained in a TSP [see page 1].*
MFS-30016

Rotary Release Mechanism With Fusible Link

The fusible link can be reused.

NASA's Jet Propulsion Laboratory, Pasadena, California

A rotary release mechanism includes a fusible rotary link made of an alloy that melts at the relatively low temperature of 60 °C. When solid, the link couples a driving shaft to a driven shaft. When necessary, the link is melted to temporarily decouple the two shafts. Upon cooling below its melting temperature, the link hardens, so that it once again couples the two shafts. This release mechanism is an extremely compact alternative to pyrotechnic release devices. The basic concept of this mechanism can be applied to such other mechanisms as pin pullers, pin pushers, electrical-disconnection mechanisms, and clutches.

The fusible link is a pellet of the low-melting-temperature alloy contained within a cavity in a housing at the coupling end of one shaft. A paddle at the coupling end of the other shaft intrudes into the pellet, so that when the pellet is solid, a firm rotary coupling exists between the two shafts (see figure). An electrical resistance heater for melting the pellet is wrapped around the housing and secured with shrink wrap. When the heater has been energized sufficiently, the pellet melts, allowing the paddle

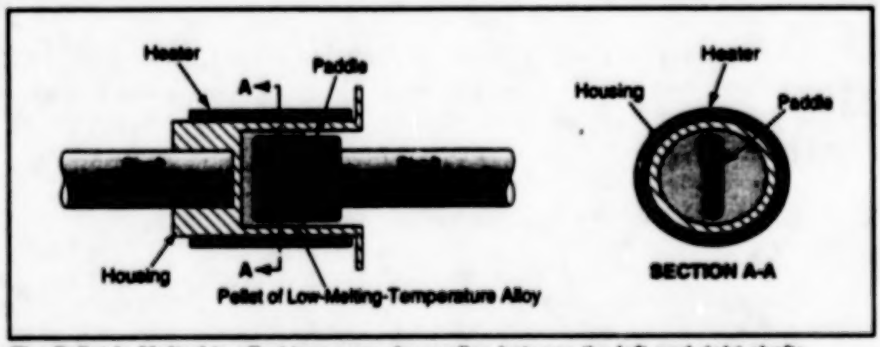

The Pellet Is Melted to effect temporary decoupling between the left and right shafts.

and its shaft to rotate freely with respect to the housing and its shaft. When the heater is shut off, the pellet cools and hardens, gripping the paddle as before.

The alloy is Cerrobend (or equivalent), which is a mixture of bismuth, lead, tin, and cadmium. In its solid state, this alloy resembles lead and can withstand a shear stress of 25 MPa. In its liquid state, this alloy exhibits the consistency and cohesiveness of mercury.

The housing is made of aluminum, which conducts heat efficiently from the heater to the pellet. The cavity in the housing is made in a slightly elliptical cross section to prevent rotary slippage between the housing and the solid pellet. The housing, pellet, and paddle can withstand torque of 17 N-m. In the original application, the paddle and the affected portions of the shafts are made of titanium to reduce the conduction of heat from the housing. Insulating material can be wrapped around the heater, housing, and nearby portions of the shafts to reduce convective and radiative losses of heat from the housing.

This work was done by Donald R. Sevilla and Richard S. Blomquist of Caltech for **NASA's Jet Propulsion Laboratory**. *Further information is contained in a TSP [see page 1].*

NPO-19579

Cross Coupling Between Attenuators in a Docking Mechanism

The capture envelope would be widened.

Lyndon B. Johnson Space Center, Houston, Texas

Cross coupling between motion attenuators on opposite sides of a docking mechanism has been proposed as a means of increasing the capture envelope. ("Capture envelope" denotes the ranges of translational and angular misalignments and rates of change of those misalignments within which the docking mechanism on one structure or vehicle can capture the mating docking mechanism on the other structure or vehicle.) The prototype system for application of the proposed cross-coupling concept is the one that was used for docking of the Apollo and Soyuz spacecraft; however, given the widespread use of docking mechanisms, the concept may prove useful in many terrestrial applications as well.

Figure 1 is a simplified illustration of the prototype docking mechanism without cross coupling. The six degrees of freedom (three translational and three rotational) of misalignment would be accommodated by six motion attenuators, which would be, essentially, combinations of springs and dampers. To provide for cross coupling, the spring-and-damper motion attenuators would be replaced by more complex attenuators. Each attenuator would contain a ball screw to convert its longitudinal extension and retraction to rotational motion, and vice versa. Each attenuator would also contain a centering spring and a hysteresis brake that could be put into a low-damping mode for capture and a high-damping mode for increased attenuation after capture.

A planetary differential would be interposed on the ball-screw shaft between the ball nut and the hysteresis brake. This differential would couple the rotary motion to one end of a flexible shaft. The other end of the flexible shaft would be connected similarly to the differential of the attenuator on the opposite side (see Figure 2). This cross coupling between attenuators on opposite sides would be

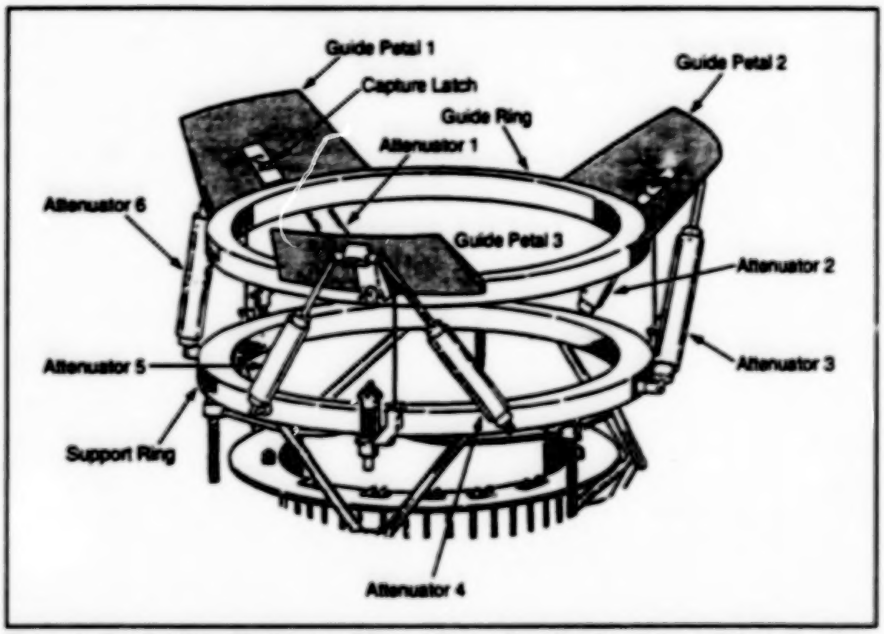

Figure 1. The Docking Mechanism Without Cross Coupling functions satisfactorily within a limited capture envelope.

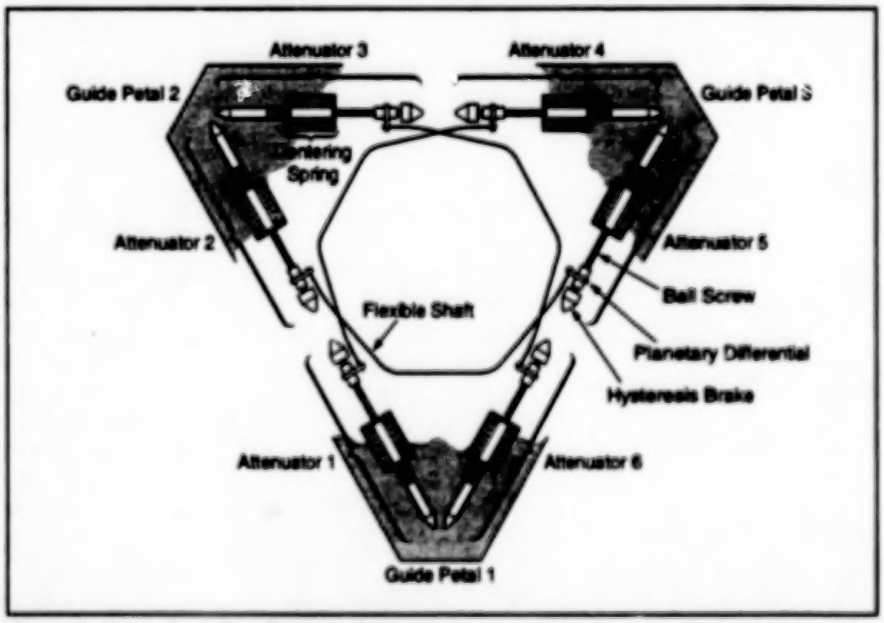

Figure 2. Cross Coupling Between Attenuators on opposite sides would divert some of the momentum and kinetic energy transferred in initial contact to generate motions that would reduce misalignment. As a result, the capture envelope would be widened.

configured to produce opposing linear motions: the extension or retraction of one attenuator would be converted into rotary motion of the flexible shaft, and the rotary motion would, in turn, be converted into retraction or extension, respectively, of the other attenuator. These complementary motions would help to remove misalignments between docking mechanisms, as in the following examples:

1. If the guide ring of the docking mechanism on the approaching vehicle made initial contact with guide petal 1 of the docking mechanism on the approached vehicle, then on the approached vehicle, attenuators 1 and 6 would be compressed, causing attenuators 3 and 4 to extend by equal amounts; this would help to remove the angular misalignment between the guide rings of the two vehicles.
2. If a guide petal of the approaching vehicle made contact with the guide ring of the approached vehicle at a location between guide petals 1 and 3, then attenuators 5 and 6 on the approached vehicle would be compressed, causing attenuators 2 and 3 to extend. As a result, guide petal 2 would be tilted upward, and misalignment between the guide rings would again be reduced.
3. Suppose that there were a large roll misalignment, such that a guide petal of the approaching vehicle made initial contact with one edge of guide petal 1 on the approached vehicle, forcing attenuator 1 to retract and attenuator 6 to extend. In this case, the cross coupling would cause attenuator 4 to extend and attenuator 3 to retract, causing the guide ring to rotate so as to reduce the roll misalignment.

This work was done by Arthur Holmberg, Matthew S. Schmidt, and Siamak Ghaffanian of Rockwell International Corp. for **Johnson Space Center.** *Further information is contained in a TSP [see page 1].*
MSC-22345

Mathematical Modeling for Control of a Flexible Manipulator

Closed-form equations account for changing inertial boundary conditions.

Marshall Space Flight Center, Alabama

An improved method of mathematical modeling of the dynamics of flexible robotic manipulators is being developed for use in controlling the motions of the manipulators. The method involves accounting for the effect, upon the modes of vibration of a manipulator, of changes in the configuration of the manipulator and the manipulated payload(s). Mathematically, these changes manifest themselves as changes in the inertial boundary conditions upon, and inertial parameters in, the differential equations of coupled vibrational, translational, and rotational motion of the manipulator and payload(s).

A flexible manipulator as contemplated here could be one that has one or more long, slender articulated link(s), like those used in outer space, but the method is also applicable to terrestrial industrial robotic manipulators with relatively short, stiff links, or to such terrestrial machines as construction cranes. Traditionally, the flexibility of long, slender links has been mathematically modeled via the assumed-modes approach. The fundamental assumption in this approach is that the boundary conditions, and hence, the eigenvalues and shapes of the vibrational modes do not vary with time. However, some maneuvers change the inertial properties in ways that change the modes significantly.

The development of the improved method began with the derivation of equations of motion for a simplified conceptual manipulator and payload; namely, a uniform beam that is pinned at one end and that supports a point mass on a rigid, massless rod at the other end (see figure). The rod can be set at an angle, θ, with respect to the y axis. Intuitively, one would expect the inertia of the rod-and-mass combination to affect the vibration of the beam to an extent that depends on θ, ranging from a maximum effect at $\theta = 0°$ to a minimum effect at $\theta = 90°$.

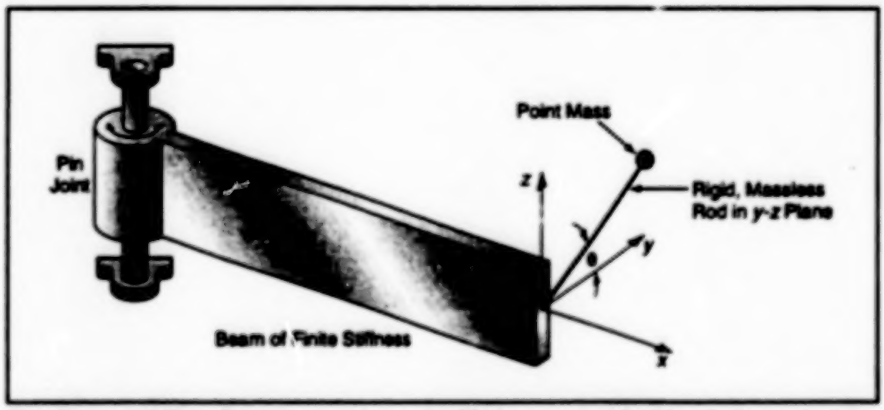

This Beam-and-Mass System served as a simplified conceptual flexible robotic manipulator and payload for purposes of initial development and assessment of the improved method.

Accordingly, closed-form equations for frequencies and shapes of vibrational modes as functions of changing inertia (more specifically, of changing θ) were derived from the equations of motion. Then, to provide for a comparison of the present method with the assumed-modes approach, two conceptual feedback control systems were tested by computational simulation. Each control system was designed to apply a time-varying torque to the pinned joint to suppress vibrations and to position the payload by rotating the beam to the desired angle.

Each control system included a linear quadratic Gaussian (LQG) controller in an outer loop and an inverse-dynamics controller in an inner loop. The designs of the controllers in one of the control systems were based on mathematical modeling of the dynamics according to the present method; those of the other control system were based on the assumed-modes approach, using $\theta = 0$. The numerical results confirmed that significant degradation of the performance of a manipulator during closed-loop control can occur if the control algorithm is derived via the assumed-modes approach and thus does not represent the changing dynamics accurately.

This work was done by Anren Hu of Dynacs Engineering Co., Inc., for **Marshall Space Flight Center.** *Further information is contained in a TSP [see page 1].*
MFS-26272

Dual-Eccentric Clevis Joint

The joint accommodates anticipated variations of dimensions.

Marshall Space Flight Center, Alabama

A redesigned clevis joint incorporates dual mating eccentric cylindrical bushings to accommodate dimensional tolerances. The use of dual eccentrics to accommodate tolerances is not new; what is noteworthy is that in this particular application, the use of dual eccentrics for this purpose makes it possible to design components associated with the clevis joint to be smaller than they would otherwise have to be.

Previously, dimensional tolerances in this application were accommodated by use of a left-hand-threaded collar that turned against a right-hand-threaded bushing. The components were designed with a total of 11 separate details and were required to be wide enough to satisfy cylinder-wall-thickness and thread-depth requirements. However, in satisfying these requirements, they violated newly imposed design limits on available space.

The dual-eccentric clevis-joint design eliminates the need for the combination of the oppositely threaded collar and bushing and, by so doing, makes the overall joint hardware fit within the available space. The dual-eccentric clevis joint (see figure) includes the usual clevis parts, plus inner and outer eccentrics and a quick-release pin. The locus of joint-axis positions defined by turning the eccentrics to all possible combinations of angular positions is a circle that contains all anticipated variations of the joint-axis positions.

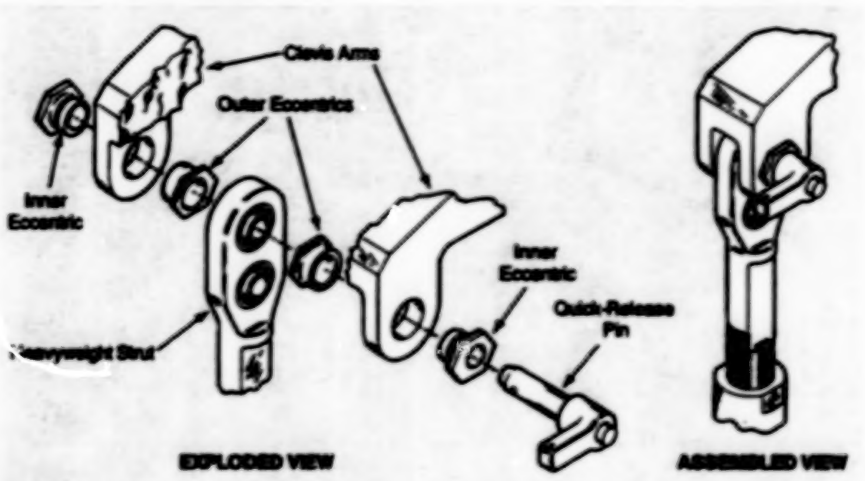

The Dual-Eccentric clevis joint and strut take up less room than did a more conventional clevis joint and a strut equipped with an oppositely threaded collar and bushing to accommodate misalignment.

During assembly, the inner eccentrics can be turned by hand to approximately align the inner hole of the clevis with the mating hole on the end of the strut. To refine the alignment, the outer eccentrics are turned, or the inner and outer eccentrics are turned simultaneously. The pin is then inserted through the clevis and the strut. A demonstration of the joint revealed that the pin forces the eccentrics on the opposite sides of the clevis to align themselves. Wrench flats on the eccentrics provide for occasions on which it becomes difficult to turn the eccentrics by hand.

This work was done by Diana L. Fairbank and John J. Sertich of Rockwell International Corp. for **Marshall Space Flight Center**. *Further information is contained in a TSP [see page 1].*

MFS-30009

BLANK PAGE

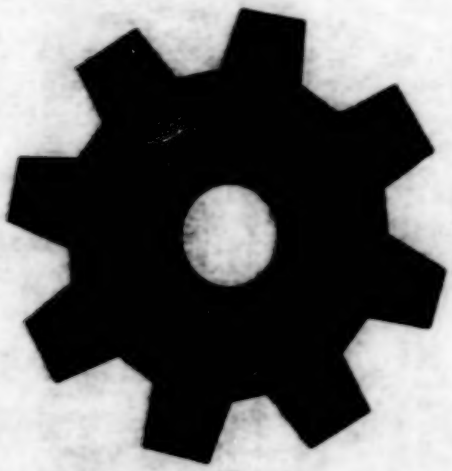

Machinery

Hardware, Techniques, and Processes

53 Apparatus Measures Thicknesses of Ice on Bars

53 Small, Lightweight Inspection Robot With 12 Degrees of Freedom

BLANK PAGE

Apparatus Measures Thicknesses of Ice on Bars

An LVDT probe translated by a stepping motor measures diameters at selected locations.

Lewis Research Center, Cleveland, Ohio

Figure 1. Ice Accumulates on nine vertical bars, the diameters of which are then measured to determine the thickness of the ice. Measurements are taken by a measuring head that travels along the measured bar on two rails parallel to the bar.

A semiautomated apparatus measures the diameters, at selected lengthwise positions, of nine vertical ice-coated bars in an icing-research wind tunnel (see Figure 1). The measurements are needed to determine the degree of uniformity of icing conditions for experiments on aircraft models. The time taken by the apparatus to measure the diameters of all nine bars at lengthwise intervals of 0.5 in. (12.7 mm) is about 1 h, and the measurements are accurate to within thousandths of an inch (hundredths of a millimeter). In contrast, a technician using a tape measure takes about two hours and obtains measurements accurate to about 1/8 in. (3 mm).

The apparatus includes a measuring head (see Figure 2) that travels on rails parallel to a bar, driven by a ball screw actuated by a stepping motor. The position of the measuring head along the bar is measured by a string potentiometer, which thus provides position feedback for a closed-loop control circuit. This circuit provides for smooth motion of the measuring head, and can be used to select various programmed sequences of motions and measurements.

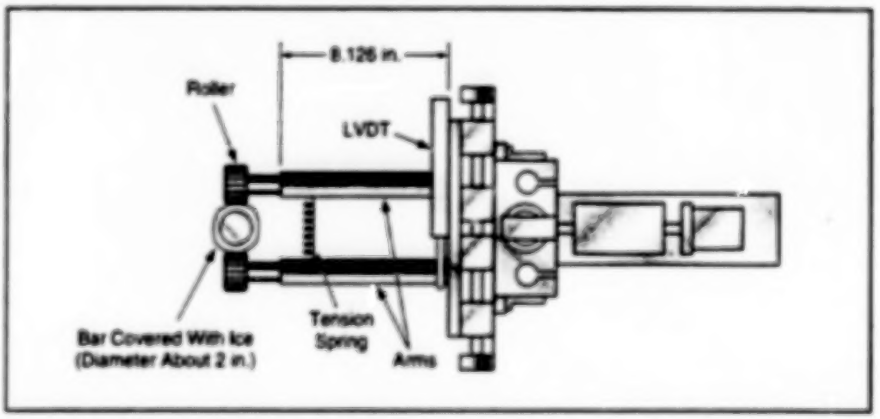

Figure 2. The Measuring Head, shown here in a simplified top view, functions essentially as a traveling, spring-loaded caliper equipped with an LVDT and rollers on the measuring tips.

As the head moves along the bar, rollers at the ends of two arms travel along opposite sides of the bar. The rollers are held to the bar by a spring between the two arms. Changes in the distance between the two rollers (changes in the diameter of the bar) are sensed by a linear variable-differential transformer (LVDT).

The output of the LVDT and the readings of the string potentiometer are recorded and processed into data on diameter (and thus thickness of ice) as a function of position along each rod. A computer can also process the data into contour plots of accretion of ice.

This work was done by Theresa L. Gibson of **Lewis Research Center** *and John M. DeArmon of Sverdrup Technology, Inc. Further information is contained in a TSP [see page 1].*

LEW-15976

Small, Lightweight Inspection Robot With 12 Degrees of Freedom

This robot can reach through openings and around obstacles.

NASA's Jet Propulsion Laboratory, Pasadena, California

The figure shows a small serpentine robot that weighs only 6 lbs (2.7 kg) and has a link diameter of 1.5 in. (38.1 mm). The robot is designed to perform inspections. Its multiple degrees of freedom enable it to reach around obstacles and through small openings into simple or complexly shaped confined spaces to positions where it could be difficult or

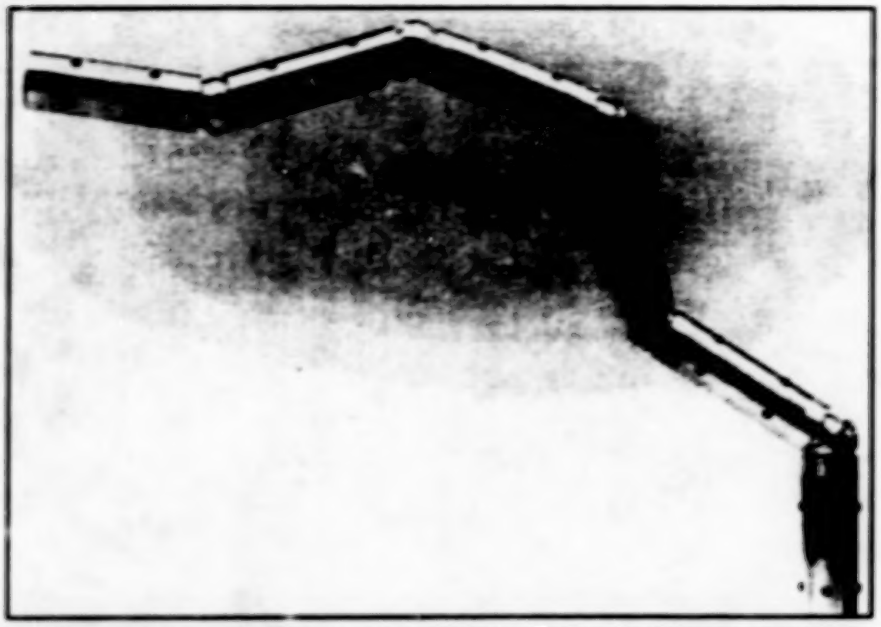

The Serpentine Inspection Robot can be mounted on the tip of the industrial robot. Motor-drive and other cables enter the serpentine inspection robot through its base, and are routed through interior openings.

even impossible to perform inspections by other means.

A fiber-optic borescope is incorporated into the robot arm, with the inspection tip of the borescope located at the tip of the robot arm. The borescope both conveys light along the robot arm to illuminate the scene to be inspected at the tip and conveys an image of the scene back along the robot arm to external imaging equipment. The robot arm acts as a flexible shield and guide tube to position the borescope. By use of a motor and cable drive within the robot, the tip of the borescope can be rotated (one of the 12 degrees of freedom) to a desired viewing angle within a 200° range.

The joints of this robot feature a unique compact design based partly on a universal-joint concept and partly on a concept of mating hemispheres, with miniature high-torque motors and gear heads with gear ratios of 1,111:1 for the upper links and 3,000:1 for the lower links mounted compactly inside the joint housings.

This is a modular serpentine robot and is designed so that sections can be readily added or removed. The motors in the joints are connected by wires to an external control and motor-drive circuits. A technician controls the movements of the robot by use of a joystick, with the help of a graphical menu on a computer video display.

This work was done by Thomas S. Lee, Timothy R. Ohm, and Samad Hayati of Caltech for **NASA's Jet Propulsion Laboratory.** *Further information is contained in a TSP [see page 1].*
NPO-19367

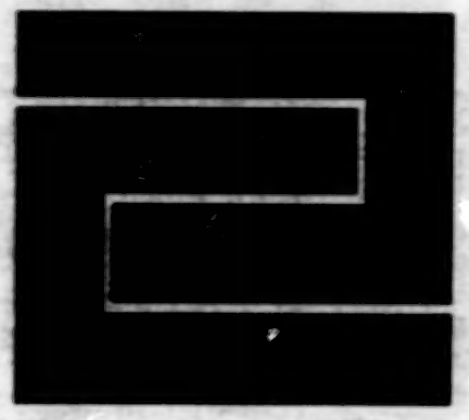

Fabrication Technology

Hardware, Techniques, and Processes

57 Alignment Jigs for Bonding End Fittings to Truss Members

BLANK PAGE

Alignment Jigs for Bonding End Fittings to Truss Members

The jigs ensure collinearity of the end fittings.

NASA's Jet Propulsion Laboratory, Pasadena, California

Figure 1 illustrates the use of a set of alignment jigs to hold fittings during adhesive bonding of the fittings to the ends of truss members. For each member, the jigs hold the two end fittings collinear while the member is allowed to move slightly, within dimensional tolerances, during injection and curing of the adhesive. Once the adhesive has been cured, the fittings remain collinear even though the member is not necessarily perfectly straight between them.

In the laboratory setting in which the alignment jigs were devised, truss members have traditionally been made from tubing, and it had been assumed that the members could be mathematically modeled as straight and subject to pure lengthwise tensile and compressive loads. In practice, tubing is not precisely straight. As a result, when end fittings are simply attached without taking special care to align them, the angle between the two end fittings on a member can give rise to significant bending moments (see Figure 2) that are not taken into account in the mathematical model of the member.

The use of the alignment jigs to ensure collinearity of end fittings helps to remove the discrepancy between the theoretical and actual loading conditions in a member. The advantage of collinear end fittings is that a lengthwise load applied to the fittings acts along their common axis. Thus, the member can be modeled mathematically, to first order, as being subjected to pure lengthwise tension or compression, without a bending moment. Of course, the nominal axial loads acting on the slight unavoidable bends in the member generate some bending moments but these are small (second- or third-order) effects.

This work was done by Lee F. Sword of Caltech for **NASA's Jet Propulsion Laboratory**. *Further information is contained in a TSP [see page 1].*

NPO-19113

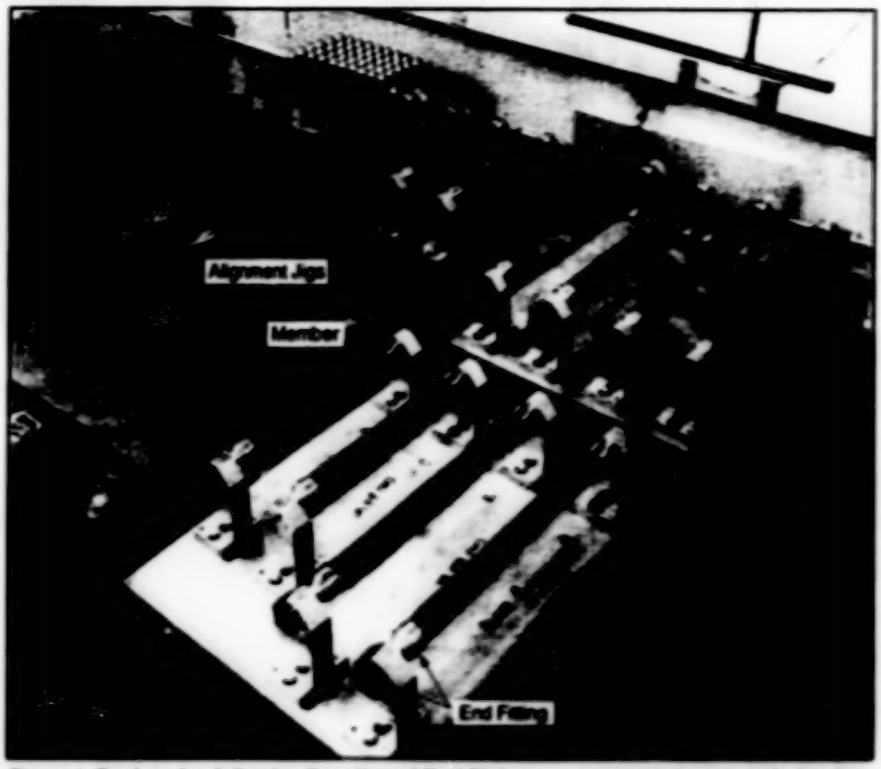

Figure 1. Devices for Adhesive Bonding of End Fittings on truss members include jigs that hold the fittings collinear until the adhesive is cured.

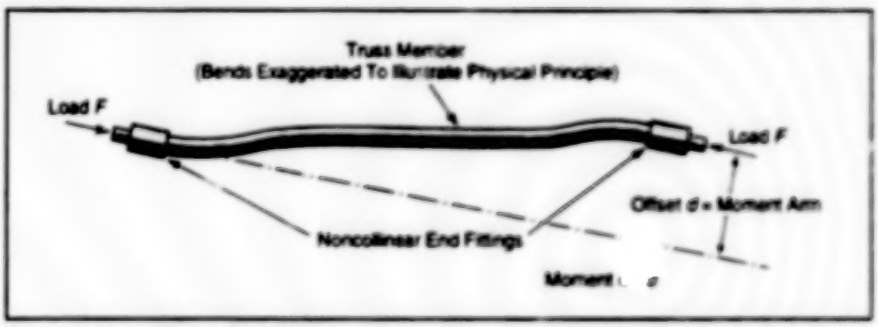

Figure 2. Noncollinear End Fittings can give rise to bending moments because the lines of action of the end loads can be offset by significant moment arms.

BLANK PAGE

Mathematics and Information Sciences

Hardware, Techniques, and Processes

61 Procedure and Criteria for Assessing CFD Codes

62 Transfer of Calibration Data via a Floppy Disk

Books and Reports

62 A* Decoding of Block Codes

BLANK PAGE

Procedure and Criteria for Assessing CFD Codes

A systematic approach to validation can help ensure good designs.

Marshall Space Flight Center, Alabama

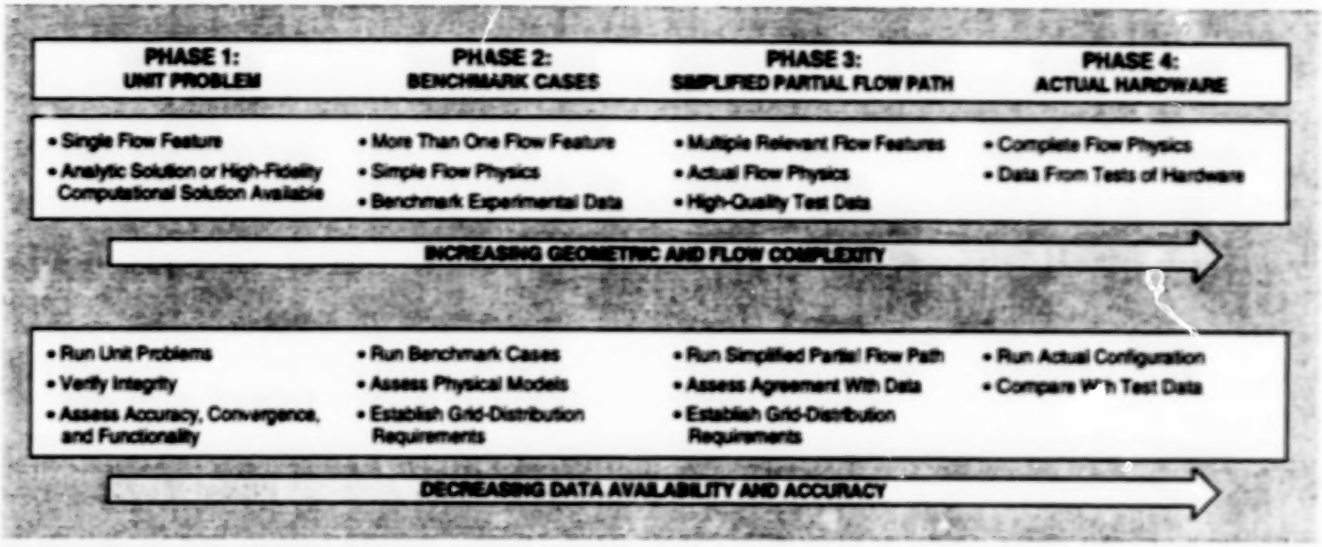
PHASE 1:
UNIT PROBLEM
PHASE 2:
BENCHMARK CASES
PHASE 3:
SIMPLIFIED PARTIAL FLOW PATH
PHASE 4:
ACTUAL HARDWARE
• Single Flow Feature
• Analytic Solution or High-Fidelity Computational Solution Available
• More Than One Flow Feature
• Simple Flow Physics
• Benchmark Experimental Data
• Multiple Relevant Flow Features
• Actual Flow Physics
• High-Quality Test Data
• Complete Flow Physics
• Data From Tests of Hardware
INCREASING GEOMETRIC AND FLOW COMPLEXITY
• Run Unit Problems
• Verify Integrity
• Assess Accuracy, Convergence, and Functionality
• Run Benchmark Cases
• Assess Physical Models
• Establish Grid-Distribution Requirements
• Run Simplified Partial Flow Path
• Assess Agreement With Data
• Establish Grid-Distribution Requirements
• Run Actual Configuration
• Compare With Test Data
DECREASING DATA AVAILABILITY AND ACCURACY

The Four Phases of the Validation Procedure represent increasing levels in the complexity of geometry and flow and, typically, decreasing availability of data.

A four-phase procedure has been devised to standardize and systematize the assessment of performances of computational fluid dynamics (CFD) software used in designing aircraft, turbines, and other machines that interact with flows. Associated with the procedure is a set of criteria by which one can classify a given computer code and measure its ability to predict flows and flow-related quantities accurately.

The procedure and criteria are tied to the engineering design cycle, providing economical means for validation of a CFD code within typical constraints of an engineering environment and thereby relieving engineers from pressure to rely on CFD codes that have not yet been thoroughly validated. The procedure and criteria are general and flexible enough to be readily applicable to a wide variety of flow-engineering problems and computer codes. With respect to a given problem, the procedure is flexible enough to provide for validation to various levels of rigor and/or sophistication, as needed. The level of validation can be incrementally upgraded as the need exists and time and funding permit.

The four phases of the procedure are illustrated schematically in the figure. Phases 1 through 4 represent increasing levels in the complexity of geometry and flow. Relevant unit problems are identified in Phase 1. "Unit problem" denotes a problem characterized by a single dominant flow feature, for which an exact solution of the equations of flow is available. In Phase 1, the CFD code is exercised on several unit problems, each of which represents one basic flow feature of the end application. In this Phase, the fundamental characteristics of the CFD are thoroughly understood and documented. Basic code methodology is considered in terms of its applicability to the problem of interest. All aspects of the code relevant to the end application are exercised to verify accuracy, functionality, and convergence characteristics. At least one unit problem is selected to test basic code logic extensively. In addition, studies of the sensitivities of computed flow quantities to changes in computational grids ("grid-sensitivity studies" for short) are performed, both to assess relative error and to provide guidance in specifying computational grids for more complex flow cases.

Relevant benchmark cases are identified in Phase 2. A benchmark case is characterized by more than one flow feature and includes basic physics relevant to the final application. Mathematical models of the relevant physics of flow within the CFD code are exercised to verify operability and to quantify accuracy relative to benchmark data. Only data from experiments of the highest quality should be used for comparisons with CFD solutions. Additional grid-sensitivity studies are conducted in this Phase to assess the level of refinement necessary to capture key physical effects. Error-assessment techniques are used as guides. Lessons learned from Phase 1 are applied in Phase 2. Fewer cases are run in Phase 2 than were run in Phase 1. A code that has been validated through Phase 2 and that satisfies all established criteria may be considered valid for use in conceptual design studies.

Test cases selected for Phase 3 are simplified versions of the final validation case. Each case in Phase 3 involves multiple geometric and flow features of the final application. Data should be selected according to defined criteria, but these criteria may be relaxed slightly if needed. An assessment of the effects of variations in topology and clustering of grids is done to provide guidance for the end application. Requirements for grids necessary to capture key physical effects are established. Relatively few test cases are considered in Phase 3. A code validated though Phase 3 may be considered valid for use in preliminary design studies.

Cases for Phase 4 should be selected from tests conducted on actual hardware. All relevant geometric and physical effects should occur simultaneously. Criteria for selection of tests should be carefully reviewed to provide for use of the best sets of data and to identify deficiencies in the data. The knowledge acquired in phases 1, 2, and 3 is applied in Phase 4.

The most appropriate physical models, best grid topology, and appropriately refined grids are used. Typically, only one or two test cases are considered in Phase 4. A code that has been validated though Phase 4 and that satisfies all established criteria may be considered valid for use in detailed design studies.

This work was done by Siyi-Jang Lin, Steven L. Barson, and Munir M. Sindir of Rockwell International Corp. for **Marshall Space Flight Center**. *Further information is contained in a TSP [see page 1].*
MFS-29972

Transfer of Calibration Data via a Floppy Disk

A system of hardware and software has been developed for a special application in which there is a need to transfer calibration data from (1) a Data General computer at an instrumentation laboratory via (2) a 3.5-in. (8.89-cm) floppy disk in IBM-PC-readable format to (3) another facility where the calibrated instruments are used. Previously, the calibration data were transferred by manual transcription, and it was desired to upgrade to automated transfer, without incurring the cost of developing the large amount of custom software that would ordinarily be needed for this purpose. The system includes an IBM-PC-compatible minicomputer that is connected to the Data General computer via an RS-232 serial link and that is configured, by use of commercial terminal-emulator software, as a remote Data General terminal. A program on the Data General computer that gains access to the data base was modified to display the requested data in the correct format on the screen. The operator runs the Data General program from the minicomputer by use of the emulator software. Upon command, the minicomputer captures the data displayed on the screen and stores them in a PC-readable file on the floppy disk.

This work was done by John P. Shonefelt and Cynthia M. Pratt of Rockwell International Corp. for **Marshall Space Flight Center**. *Further information is contained in a TSP [see page 1].*
MFS-30097

Books and Reports

A* Decoding of Block Codes

A report presents a study of the application of the A* algorithm to maximum-likelihood soft-decision decoding of binary linear block codes. The A* algorithm is an artificial-intelligence algorithm that finds a path in a finite-depth tree that is optimum in the sense that the choice of path maximizes a function. In this application, the tree is the binary tree that represents decoding decisions between zeros and ones, and the function to be maximized is the likelihood function of the received sequence of symbols, given each code word. The algorithm considers code words one bit at a time, making use of the most reliable received symbols first and pursuing only the partially expanded code words that might be maximally likely. In the study, a version of the A* algorithm for maximum-likelihood decoding of block codes is implemented for block codes up to 64 bits long. The efficiency of this algorithm makes simulations of codes with lengths up to 64 feasible. The report details the implementation, compares the complexity of decoding by use of this version of the A* algorithm with that of exhaustive-search and Viterbi decoding algorithms, and presents performance curves obtained with this version of the A* algorithm for several codes.

This work was done by Laura Ekroot and Samuel J. Dolinar, Jr., of Caltech for **NASA's Jet Propulsion Laboratory**. *To obtain a copy of the report, "A* Decoding of Block Codes," see TSP's [page 1].*
NPO-19572

Life Sciences

Hardware, Techniques, and Processes

65 Semiautomated Motility Assay for Determining Toxicity

66 Cultivating Insect Cells To Produce Recombinant Proteins

BLANK PAGE

Semiautomated Motility Assay for Determining Toxicity

Computer processing of images of swimming protozoa quickly yields documentation of toxicity.

Marshall Space Flight Center, Alabama

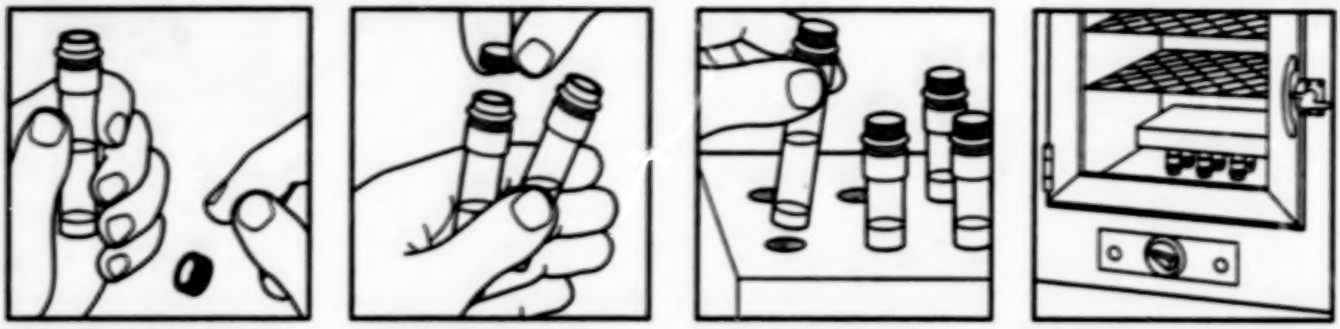

1. Use scissors to open foil pouch. Discard colored cap from rehydration-fluid vial.
2. Transfer colorless cap onto rehydration-fluid vial.
3. Insert vial into foam rack.
4. Invert foam rack and incubate 10 minutes at 35 to 37 °C.

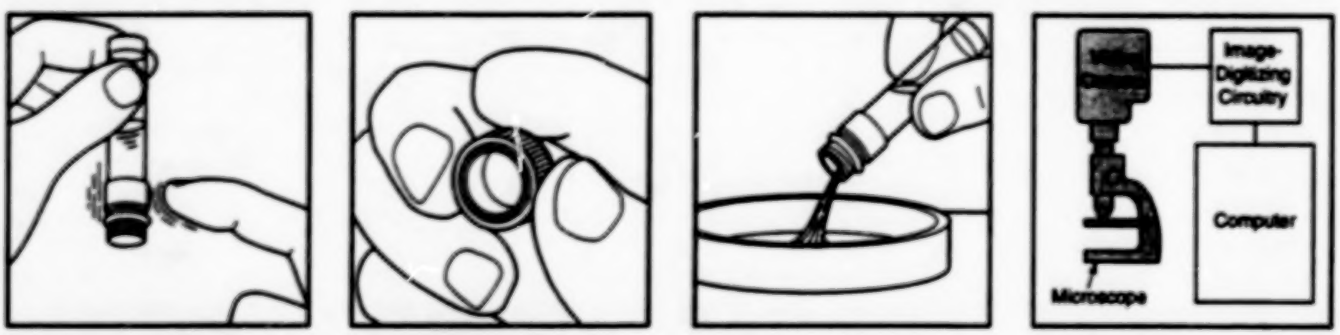

5. Remove vial from rack. Shake vial vigorously to disperse microorganisms.
6. Remove cap and look at inside surface to be certain that no undissolved black particles are present.
7. Decant entire contents into petri dish.
8. Analyze sample

Freeze-Dried Protozoa From a Kit are rehydrated and incubated, then placed in a petri dish, where they are exposed to the material to be tested for toxicity.

An improved method of assessing the toxicities of various substances is based on observation of the effects of those substances on the motilities of a manageably small number of cells of the protozoan species *Tetrahema pyriformis*. The method provides a rapid and economical alternative to the Draize test, in which the toxicity of a substance is measured in terms of its effects on the eyes of living rabbits. The method provides repeatable, standardized tests with minimal handling by technicians and with minimal exposure of technicians to chemicals.

A previous article in *NASA Tech Briefs* described the determination of toxicity by observation of macroscopic patterns formed by large numbers of *Tetrahema pyriformis* organisms swimming in culture media containing toxins diluted in various degrees. The article was "Bioconvective Assay as Alternative to Draize Test" (MFS-26162), Vol. 17, No. 2 (February 1993), page 95. As described in more detail in that article, equipment for a bioconvective assay can be packaged in a kit that is stored under refrigeration to preserve a slant culture of the protozoa. Although a bioconvective assay is convenient in comparison with older techniques for determining toxicity, it still consumes a considerable amount of time (several days).

Like the bioconvective-assay method, the present method involves the use of a kit to prepare a culture of *Tetrahema pyriformis* and expose it to a toxin, but in this case, the preparation time is much shorter. Freeze-dried *Tetrahema pyriformis* cells are rehydrated and incubated for 10 minutes at a temperature of 35 to 37 °C (see figure). Then the mixture of cells and rehydration fluid is decanted into a petri dish that contains a medium with the appropriately diluted material to be tested for toxicity. A sample from the petri dish is placed under a microscope equipped with phase-contrast or dark-field optics and a video camera.

A live or videotaped sequence of video images of 50 or more single cells of *Tetrahema pyriformis* is digitized and analyzed by a computer to identify the cells, measure their concentration, and characterize their motility in terms of velocity and linearity. (Degradation of motility is an indication of toxicity.) The data from this analysis can be stored or printed out immediately to provide quick documentation of toxicity.

This work was done by David A. Noever and Raymond Cronise of **Marshall Space Flight Center.** *Further information is contained in a TSP [see page 1].*

MFS-28906

Cultivating Insect Cells To Produce Recombinant Proteins

Cells are grown in a rotating bioreactor and infected with viruses containing selected genes.

Lyndon B. Johnson Space Center, Houston, Texas

A method of producing recombinant proteins involves (1) the growth of insect cells in a nutrient solution in a cylindrical bioreactor rotating about its cylindrical axis, which is oriented horizontally and (2) infecting the cells with viruses into which genes of a selected type have been cloned. The genes in question are those that encode the production of the desired proteins.

One reason for choosing insect cells for this method is that like most other animal cells, insect cells are versatile enough to produce a wide variety of functional proteins. Another reason is that in comparison with other animal cells, insect cells are highly productive in this regard; they are capable of producing protein products at concentrations that range from 1 to more than 500 mg/L.

The insect-cell line used initially in this method is that of the ovary of the lepidopteran known popularly as the fall armyworm and more technically as *Spodoptera frugiperda* ("Sf9" for short). The Sf9 cell line was selected for a number of reasons, including that (1) its characteristics are well-known from prior intensive research, (2) it is commercially available, (3) it is an immortal cell line, (4) the cells of this line grow more robustly than other insect cells do, and (5) Sf9 readily accepts foreign genes that code for recombinant proteins because it is very receptive to infection by, and replication of, viruses.

The viruses used initially in this method are baculoviruses, which are not hazardous to humans and other vertebrates but are pathogenic toward some species of insects (including Sf9), in which they cause cell lysis. (Baculoviruses are the active ingredients in some insecticides.)

As explained in several articles in prior issues of *NASA Tech Briefs*, horizontal rotating bioreactors have been developed to provide nutrient-solution environments conducive to the growth of delicate animal cells, with gentle, low-shear flow conditions that keep the cells in suspension without damaging them. The horizontal rotating bioreactor preferred for use in this method, denoted by the acronym "HARV," was described in "High-Aspect-Ratio Rotating Cell-Culture Vessel" (MSC-21662), *NASA Tech Briefs*, Vol. 16, No. 5 (May, 1992), page 150.

The protein β-galactosidase (β-Gal) has been chosen as a model protein to produce in experiments directed toward further development of the method. This protein is frequently used in Sf9 studies because it is readily available and can be readily assayed. A mutant form of the baculovirus *Autographa californica* containing the gene that codes for β-Gal is used as a cloning vector to introduce and express the β-Gal gene in Sf9 cells. As the virus replicates, the β-Gal gene is expressed along with production of native viral proteins.

The use of the HARV (as distinguished from other bioreactors) offers the potential to enhance production in a number of ways. Because the HARV cultures Sf9 cells to densities larger than those achievable in prior bioreactors, the overall production per unit volume may be correspondingly greater. The low-turbulence flow field in the HARV may enhance infectivity by promoting adherence of viruses to cells. The environment in the HARV may also enhance the metabolism of the cells in such a way as to increase gene transcription, protein translation, post-translational processes, and secretion of protein from the cells.

This work was done by Glenn Spaulding of **Johnson Space Center**, *Thomas Goodwin and Tacey Prewett of KRUG Life Sciences, and Angela Andrews, Karen Francis, and Kim O'Connor of Tulane University. Further information is contained in a TSP [see page 1].*

Inquiries concerning rights for the commercial use of this invention should be addressed to the Patent Counsel, Johnson Space Center [see page 1]. Refer to MSC-22336.

END

09-13-96